




Kinematics of stellar substructures in the small magellanic cloud

Dalal El Youssoufi ^{1,2}, Maria-Rosa L. Cioni ¹★, Nikolay Kacharov,¹ Cameron P. M. Bell ¹, Gal Matjević,¹ Kenji Bekki,³ Richard de Grijs,^{4,5} Valentin D. Ivanov⁶ and Jacco Th. van Loon⁷

¹Leibniz-Institut für Astrophysik Potsdam, An der Sternwarte 16, D-14482 Potsdam, Germany

²Institut für Physik und Astronomie, Universität Potsdam, Haus 28, Karl-Liebknecht-Str. 24/25, D-14476 Golm (Potsdam), Germany

³ICRAR, M468, The University of Western Australia, 35 Stirling highway, Crawley, WA 6009, Australia

⁴School of Mathematical and Physical Sciences, Macquarie University, Balaclava Road, Sydney, NSW 2109, Australia

⁵Research Centre for Astronomy, Astrophysics and Astrophotonics, Macquarie University, Balaclava Road, Sydney, NSW 2109, Australia

⁶European Southern Observatory, Karl-Schwarzschild-Str. 2, D-85748 Garching bei München, Germany

⁷Lennard-Jones Laboratories, Keele University, ST5 5BG, UK

Accepted 2023 April 27. Received 2023 April 24; in original form 2022 November 17

ABSTRACT

We present a kinematic analysis of the Small Magellanic Cloud using 3700 spectra extracted from the European Southern Observatory archive. We used data from *Gaia* and near-infrared photometry to select stellar populations and discard Galactic foreground stars. The sample includes main-sequence red giant branch and red clump stars, observed with Fibre Large Array Multi Wavelength Spectrograph. The spectra have a resolving power $\lambda/\Delta\lambda$ from 6500 to 38 000. We derive radial velocities by employing a full spectrum fitting method using a penalized pixel fitting routine. We obtain a mean radial velocity for the galaxy of $159 \pm 2 \text{ km s}^{-1}$, with a velocity dispersion of $33 \pm 2 \text{ km s}^{-1}$. Our velocities agree with literature estimates for similar (young or old) stellar populations. The radial velocity of stars in the Wing and bar-like structures differ as a consequence of the dynamical interaction with the Large Magellanic Cloud. The higher radial velocity of young main-sequence stars in the bar compared to that of supergiants can be attributed to star formation around 40 Myr ago from gas already influenced by tidal stripping. Similarly, young main-sequence stars in the northern part of the bar, resulting from a prominent star forming episode 25 Myr ago, have a higher radial velocity than stars in the southern part. Radial velocity differences between the northern and southern bar overdensities are also traced by giant stars. They are corroborated by studies of the cold gas and proper motion indicating stretching/tidal stripping of the galaxy.

Key words: techniques: radial velocities – galaxies: interactions – Magellanic Clouds – galaxies: stellar content.

1 INTRODUCTION

The Small Magellanic Cloud (SMC) is a dwarf irregular galaxy, located at $\sim 60 \text{ kpc}$ (de Grijs & Bono 2015) and characterized by a gas rich and low metallicity environment. Together with the Large Magellanic Cloud (LMC), it represents the nearest interacting pair of dwarf galaxies to the Milky Way (MW). The pair has been heavily influenced by dynamical interactions of tidal and/or ram pressure nature and has likely experienced a collision $\sim 200 \text{ Myr}$ ago leading to the formation of the Magellanic Bridge (e.g. Yoshizawa & Noguchi 2003; Diaz & Bekki 2012; Kallivayalil et al. 2013; Zivick et al. 2019; Schmidt et al. 2020) and $\sim 2 \text{ Gyr}$ ago leading to the formation of the Magellanic Stream (e.g. Mathewson, Cleary & Murray 1974; Nidever, Majewski & Butler Burton 2008; D’Onghia & Fox 2016).

The structure of the SMC reflects its complex dynamical H I story where different stellar populations show different features along the line of sight. The galaxy is characterized by an elongated bar-like (bar hereafter) structure along the North–East–South–West (NE–SW) axis (e.g. de Vaucouleurs & Freeman 1972; Subramanian & Subramaniam

2012; Jacyszyn-Dobrzniecka et al. 2016; Scowcroft et al. 2016; Ripepi et al. 2017) and an eastern Wing towards the Magellanic Bridge (Shapley 1940). Young stellar populations follow the irregular and asymmetric distribution typical of the H I gas (e.g. Stanimirović, Staveley-Smith & Jones 2004; Di Teodoro et al. 2019) while older stellar populations depict an elliptical/spheroidal distribution (e.g. Cioni, Habing & Israel 2000; Zaritsky et al. 2000; Rubele et al. 2015; El Youssoufi et al. 2019).

El Youssoufi et al. (2019, 2021) used photometric data from the Visible and Infrared Survey Telescope for Astronomy (VISTA; Sutherland et al. 2015), survey of the Magellanic Clouds system (VMC; Cioni et al. 2011), and the VISTA Hemisphere Survey (VHS; McMahon et al. 2013) to obtain a comprehensive morphological view of the Magellanic Clouds and their periphery by tracing stellar populations of different median ages. El Youssoufi et al. (2019) provided the highest spatial resolution maps of the main bodies of the Magellanic Clouds in the near-infrared (NIR) to date. They found that young main-sequence stars in the SMC delineate a broken bar while red clump (RC) as well as red giant branch (RGB) stars display signatures of elongations towards the Magellanic Bridge, also detected by Belokurov et al. (2017) and Muraveva et al. (2018), due to a LMC–SMC interaction $\sim 200 \text{ Myr}$ ago. Irregular central features,

* E-mail: mcioni@aip.de

showing that the inner SMC has been affected by tidal disruption, were also evidenced from the distribution of intermediate-age/old stars (1–7 Gyr old); they include two main overdensities along the NE–SW axis.

Pieres et al. (2017) identified an overdensity (SMCNOD) eight degrees from the centre of the SMC, mainly comprised of intermediate-age (a few Gyr old) stars, which were probably removed from the SMC disc by tidal stripping. El Youssofi et al. (2021) discovered another substructure in the vicinity of SMCNOD, Northern Substructure 2, lying at a similar distance as the SMC and located seven degrees NE of the centre; the substructure is probably associated with the ellipsoidal shape of the galaxy and is also comprised of intermediate-age stars. The shell substructure, located at about two degrees from the centre of the SMC in the NE direction is mainly composed of young (~ 150 Myr old) stars suggesting it formed during a recent star formation event as no evidence was found of a tidal origin (Martínez-Delgado et al. 2019).

The outskirts of the SMC appear highly disturbed with tails connected to the Old Bridge, a tail of stars offset from the gaseous Bridge (Belokurov et al. 2017; Mackey et al. 2018; El Youssofi et al. 2021). The SMC is also characterized by a line-of-sight depth that can reach ~ 30 kpc depending on the type of stellar tracer (e.g. Subramanian & Subramaniam 2012; Jacyszyn-Dobrzyniecka et al. 2016, 2017; Ripepi et al. 2017; Muraveva et al. 2018). Furthermore, a foreground population manifesting itself as a bimodality in RC distances has been measured ~ 11 kpc in front of the SMC’s main body (e.g. Nidever et al. 2010; Subramanian et al. 2017; El Youssofi et al. 2021; Omkumar et al. 2021). This is likely a perturbed population formed at smaller SMC radii and driven outwards (Cullinane et al. 2023). The complex nature of the structure of the SMC is also emphasized by filaments, arcs and shells in the distribution of H I gas (e.g. Stanimirović et al. 2004; Di Teodoro et al. 2019). Pingel et al. (2022) provided the most sensitive and detailed view of H I emission associated with the SMC, showing details on scales from 10 pc to 5 kpc.

Spectroscopic observations have made significant contributions to the measurement of stellar motions leading to a greater understanding of galaxy kinematics, formation and evolution. Our knowledge of radial velocities (RVs) of SMC stars has been limited to modest stellar samples from a few types of tracers such as luminous supergiants (Ardeberg & Maurice 1977, 1979), Cepheids (Mathewson, Ford & Visvanathan 1988), carbon stars (Hardy, Suntzeff & Azzopardi 1989; Hatzidimitriou et al. 1997; Kunkel, Demers & Irwin 2000), RC stars (Hatzidimitriou, Cannon & Hawkins 1993), and RGB stars (Suntzeff et al. 1986). More recently, the kinematics of RC and RGB stars in the periphery of the galaxy have been mapped by the Magellanic Edges Survey (Cullinane et al. 2020).

Harris & Zaritsky (2006) provided the first large spectroscopic survey of RGB stars in the SMC and derived a velocity gradient of $8.3 \text{ km s}^{-1} \text{ deg}^{-1}$. They also concluded that the SMC is supported by its velocity dispersion rather than by rotation. Evans & Howarth (2008) undertook a large spectroscopic survey of massive stars in the SMC. They obtained a local velocity dispersion similar to that of RGB stars ($\sigma = 30 \text{ km s}^{-1}$), however, unlike Harris & Zaritsky (2006), they found evidence of rotation with a mean velocity gradient of $26.3 \pm 1.6 \text{ km s}^{-1} \text{ deg}^{-1}$ at $\text{PA} = 126.2 \pm 3.9 \text{ deg}$. Dobbie et al. (2014) used a large sample of RGB stars to study the kinematics of the SMC, and detected signatures of rotation with an observed rotation curve between $20\text{--}40 \text{ km s}^{-1}$ at similar position angles ($120\text{--}130 \text{ deg}$) to Evans & Howarth (2008). Additionally, Dobbie et al. (2014) found evidence of tidal stripping in the outer SMC. De Leo et al. (2020) used a sample of red giants and found significant tidal

disruption in the inner 2 kpc of the SMC using a combination of proper motion (PM) and RV measurements, but with no obvious signature of rotation. Stanimirović et al. (2004) obtained one of the first rotation measurements in H I using RVs with a maximum velocity of 50 km s^{-1} , a mean PA of 40 deg and a velocity dispersion of about 22 km s^{-1} . These results were confirmed by Di Teodoro et al. (2019) using spatially higher resolution observations of H I in the SMC. Differences in velocity dispersion of stars from different stellar populations result also from chemodynamical simulations of the SMC, LMC, and the Galaxy (e.g. Bekki & Chiba 2009). In a first instance, the apparent gradient in RV is of the same order of magnitude as the velocity dispersion and the rotation amplitude which means that bulk motion and rotation cannot be inferred independently from RV data alone.

Until recently, advances made by spectroscopic studies were mostly constrained to one dimensional RVs, highlighting the importance of PMs for a comprehensive understanding of the three-dimensional (3D) kinematics, and dynamics of the galaxies. The *Hipparcos* satellite provided one of the first PM measurements in the SMC (Kroupa & Bastian 1997), the sample, however, was limited to eleven massive stars and the uncertainties were of the order of ~ 65 per cent. Observations with the *Hubble Space Telescope* (*HST*) by Kallivayalil et al. (2006) measured the PM of the SMC to an accuracy of 15 per cent allowing the determination of the PM of the centre of mass of the galaxy and showcasing that the Magellanic Clouds are most likely on their first infall towards the MW or are on a long eccentric orbit. Subsequently, Kallivayalil et al. (2013) reduced the PM uncertainties to 1–2 per cent by increasing the time baseline with additional *HST* observations, but no conclusion could be reached about the rotation of the galaxy perhaps due to the small number of targeted fields. No evident rotation in the plane of the sky was also found by van der Marel & Sahlmann (2016) using PMs for eight stars from the Tycho–*Gaia* astrometric solution (TGAS) Catalogue, which contains PMs only for stars in common between *Gaia* Data Release 1 (DR1; Gaia Collaboration et al. 2016) and the *Hipparcos* Tycho–2 Catalogue.

Oey et al. (2018) used *Gaia* DR2 PMs in combination with RVs from the Runaways and Isolated O-Type Star Spectroscopic Survey of the SMC (RIOTS4; Lamb et al. 2016) and concluded that the bar and Wing of the SMC are kinematically distinct features, with the Wing having a consistent transverse motion along the Bridge towards the LMC. Results by Murray et al. (2019) showed that the 3D kinematics of a sample of young massive stars (their RV follows that of the H I gas) is inconsistent with disc rotation in the SMC. Niederhofer et al. (2018) used ground-based VMC observations to present the first stellar resolved PM map of the SMC. This map revealed a non-uniform velocity pattern indicative of a tidal feature behind the main body of the galaxy and a flow of stars along the line-of-sight. Zivick et al. (2019) and Schmidt et al. (2020) studied the kinematics of the Magellanic Bridge and confirmed that old and young stellar populations are moving away from the SMC towards the LMC. Additionally, Niederhofer et al. (2021) suggested a dynamical stretching of the galaxy with ordered motion of intermediate-age/old stars from the SMC towards the Old Bridge, as well as a stellar motion in the North which might be related to the Counter Bridge (Diaz & Bekki 2012). Grady, Belokurov & Evans (2021) found evidence of tidal stripping in the SMC both in PM and metallicity space. The density and velocity flow of stars from the SMC to the LMC along the Bridge is traced by *Gaia* Early Data Release 3 (EDR3) data globally and separately for young and evolved stellar populations (Gaia Collaboration et al. 2021b). A best-fitting model of the SMC kinematics, based on *Gaia* DR2, highlights

the need to distinguish among the different stellar populations once sufficiently populated and widely distributed RV samples become available (Zivick, Kallivayalil & van der Marel 2021).

The aim of this paper is to use available spectra from the European Southern Observatory (ESO) Science Archive Facility (SAF) to increase the sample of RVs and characterize the kinematics of the morphological features belonging to the SMC and its vicinity. The paper is organized as follows: in Section 2, we describe the used data sets and sample selection; we outline the method and steps involved in obtaining RVs in Section 3 and we describe our results in Section 4, while in Section 5, we summarize our main conclusions and future prospects.

2 SAMPLE SELECTION

To select a sample of stars for which to search the ESO SAF for available spectra, we used NIR photometry from the VMC survey and VHS. We distinguished between stars belonging to different stellar populations as in El Youssoufi et al. (2019), using regions in the colour–magnitude diagram (CMD) with different median ages and evolutionary stages. Additionally, we used Two Micron All Sky Survey (2MASS; Skrutskie et al. 2006) photometry for objects that are too bright for the VISTA surveys. The ESO SAF provides access to data acquired with ESO telescopes. Raw, processed, and catalogued data can be queried via different web query interfaces. In our work, we used the spectral query form.¹ that gives access to reduced spectral ESO phase 3 data products. In the following subsections, we outline our selection criteria for both the photometric and spectroscopic data sets as well as describe the parameters encompassed by the spectroscopic sample.

2.1 Photometric data

The VMC survey and VHS are multiband photometric surveys carried out using the VISTA infrared camera (VIRCAM; Dalton et al. 2006; Emerson, McPherson & Sutherland 2006). We used observations in the J and K_s bands within a 10 deg radius from the SMC’s optical centre, Right Ascension (RA)=13.05 deg and Declination (Dec.) = -72.83 deg at the epoch J2000 (de Vaucouleurs & Freeman 1972). The VMC data were acquired between 2010 February and 2016 November and were released as part of Data Release 5 (DR5) of the VMC survey² VMC observations reach 5σ point source limits of $J = 22$ mag and $K_s = 21.5$ mag (in the Vega system) across an area of ~ 43 deg² on the SMC component of the survey. The median full width at half maximum (FWHM) of point-like sources in the VMC images corresponds to 1 arcsec in J and 0.93 arcsec in K_s . Beyond this area, VHS observations reach 5σ limits of $J = 19.3$ mag and $K_s = 18.5$ mag (also in the Vega system). The median FWHM of point-like sources in the VHS images corresponds to 0.99 arcsec in J and 0.91 arcsec in K_s . VHS observations obtained until 2017 March 30th were released as part of DR5 of the VHS survey,³ whereas for VHS observations obtained until 2017 September 30th only raw images are publicly available. VMC and VHS images were initially processed by the Cambridge Astronomical Survey Unit (CASU) using the VISTA Data Flow System (Emerson et al. 2006) and further processed by the Wide Field Astronomy Unit (WFAU) as well as stored and made available

to the community at the VISTA Science Archive (VSA; Cross et al. 2012). We used the aperture corrected magnitudes calculated within a 2 arcsec diameter (`jAperMag3` and `ksAperMag3`), as these are the most reliable magnitudes for point sources, from the `vmcsource` and `vhssource` tables. These magnitudes were calibrated as outlined by González-Fernández et al. (2018). VMC and VHS observations overlap in the area of the Magellanic Bridge and around the SMC. We eliminated duplicate sources by keeping the VMC sources because VMC data are deeper than the VHS data. Our initial selection criteria refer to detections in both J and K_s bands for objects that have at least a 70 percent probability of being stars (`flag mergedClass = -1` or `-2`), as well as with photometric uncertainties better than 0.1 mag in both bands. Furthermore, we only selected sources with minor quality issues (`flag ksppErrBits ≤ 256` and `jppErrBits ≤ 256`). Applying these criteria, we obtained 3407 966 sources.

2MASS data across the SMC were obtained from a dedicated 1.3 metre telescope at the Cerro Tololo Inter-American Observatory. They correspond to a sensitivity of $J = 15.8$ mag and $K_s = 14.3$ mag (in the Vega system) at a signal-to-noise ratio (SNR) of 10. The median FWHM of the 2MASS images corresponds to 2.9 arcsec in both J and K_s . However, multiple dithered observations improved the spatial resolution of the images. 2MASS observations were acquired between 1997 June and 2001 February. The data were downloaded from the Gaia@AIP portal⁴ We required that the objects were detected in both bands, with photometric uncertainties smaller than 0.05 mag, and quality flags applied to the J , H , and K_s bands (we included the H band to obtain a more reliable sample), as follows: photometric quality flag (`flag ph_qual`) = AAA, reflecting detections where valid measurements were made with a SNR > 10 and photometric errors below 0.1 mag, Read flag (`flag rd_flg`) = 222 indicating that the default magnitude is derived from a profile-fitting measurement made on six individual 1.3 s exposures covering the sources, blend flag (`flag rd_flg`) = 111, indicating that one component was fit when estimating the brightness of the source, contamination and confusion flag (`flag cc_flg`) = 000, where only sources unaffected by known artifacts are kept. In total, 27 716 sources were selected, excluding sources in common with the VISTA sample. We note that the difference between the filter systems (e.g. Cioni et al. 2011; González-Fernández et al. 2018) does not influence our study.

We combined data from *Gaia* EDR3 (Gaia Collaboration et al. 2021a) with the NIR samples because the astrometric solution (RA and Dec. – position on the sky, ω – parallax, μ_{RA} and μ_{DC} – proper motion) allowed us to reduce the number of MW foreground stars. *Gaia* EDR3 data are based on observations collected during the first 34 months of the mission which started in 2013 December. They include objects with a limiting magnitude of $G = 21$ mag (in the Vega system). We performed the cross-correlation between *Gaia* EDR3, VMC, and VHS data to retain sources within a distance of 1 arcsec. The cross-match of *Gaia* EDR3 and 2MASS is provided by the *Gaia* Data Processing and Analysis Consortium. The selection criteria we applied to maximize the number of SMC stars are the following: $\omega \geq 0.2$ mas, $-4 \leq \mu_{Dec.} \leq 2$ mas yr⁻¹ and $-2.5 \leq \mu_{RA} \leq 4.5$ mas yr⁻¹. The parallax criterion is the same as in El Youssoufi et al. (2021) whereas the proper motion criteria encompass also the diffuse component around the galaxy. These criteria remove bright main-sequence and giant stars of the MW (e.g. Vasiliev 2018), but due to the uncertainties of parallax and proper motion at the distance

¹https://Archive.eso.org/wdb/wdb/adp/phase3_spectral/form

²<https://www.eso.org/sci/publications/announcements/sciann17232.html>

³<https://www.eso.org/sci/publications/announcements/sciann17290.html>

⁴<https://gaia.aip.de/>

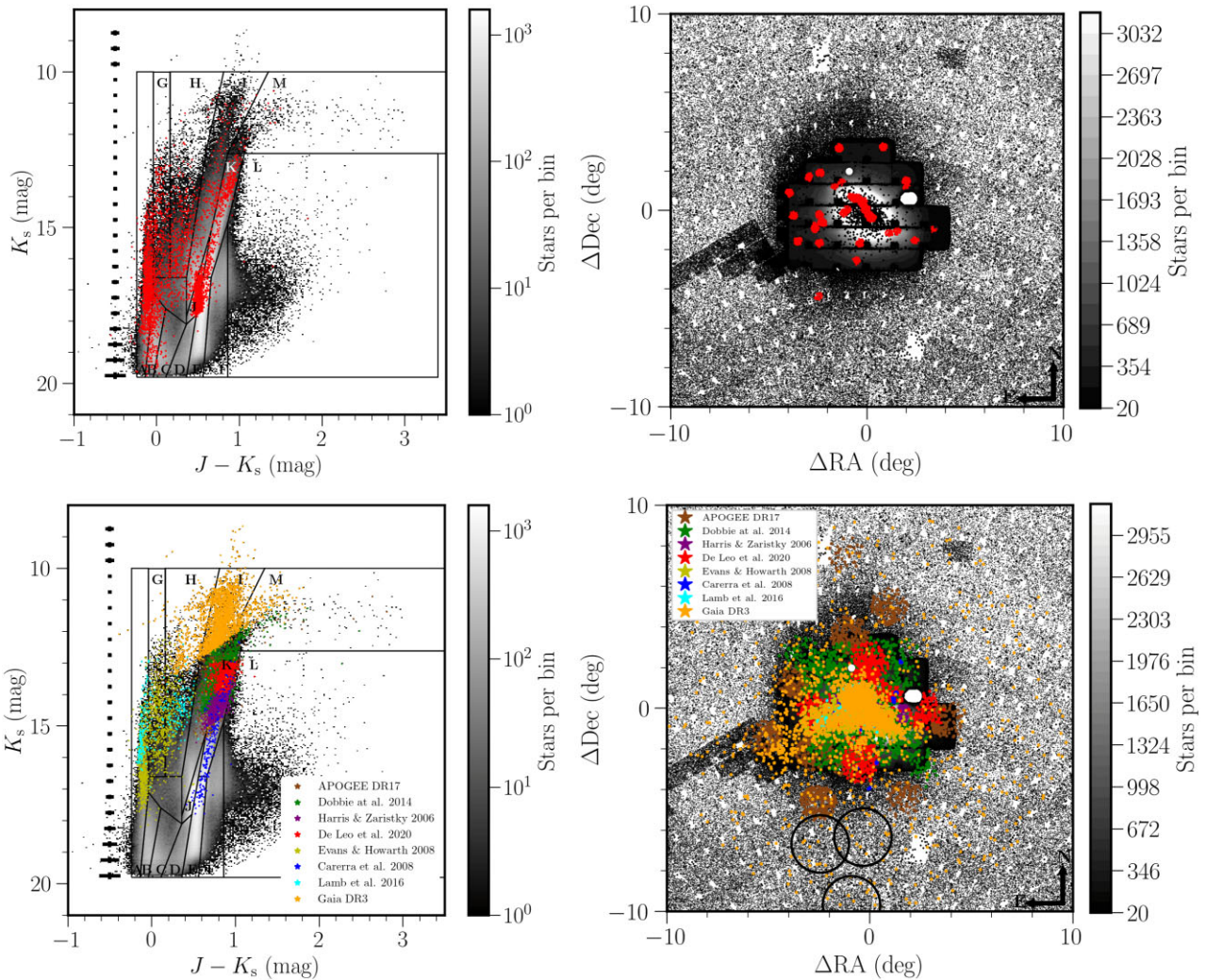


Figure 1. (top left) NIR ($J - K_s$, K_s) Hess diagrams of the SMC stars after the cross-match with *Gaia* EDR3 data. The grey scale indicates the stellar density on a logarithmic scale whereas horizontal bars show the photometric uncertainties as a function of magnitude. VMC, VHS, and 2MASS photometry is used. Points in red refer to stars with available spectra in the ESO archive, after applying the selection criteria discussed in Section 2. Boxes outline the stellar population regions as in El Yousoufi et al. (2019). (top right) Spatial distribution of SMC stars. The stellar clusters 47 Tuc and NGC 362, at $(\Delta RA, \Delta Dec.)$ of $(2.1 \text{ deg}, 0.6 \text{ deg})$ and $(-0.9 \text{ deg}, 1.96 \text{ deg})$, respectively, have been excluded using circular masks. Rectangular regions of high stellar density represent the location of VMC tiles. The overdensity at $(\Delta RA, \Delta Dec.)$ of $(5 \text{ deg}, 8 \text{ deg})$ corresponds to a tile in the Magellanic Stream component of the VMC survey. The gaps at the bottom of each VISTA tile refer to the excluded detector #16. The grey scale indicates the stellar density per deg^2 , with (red) and without available spectra in the ESO archive. (bottom left and right) As figures in the upper panels but with points in colour referring to stars with available spectra in different literature studies. Circles to the extreme outskirts encompass the regions studied using data from the Magellanic Edges Survey (Cullinane et al. 2023).

of the SMC do not allow us to distinguish MW stars among the faint sources. In total, 1931 462 sources were removed from our sample based on these criteria.

Furthermore, we used the Optical Gravitational Lensing Experiment (OGLE) III (Soszyński et al. 2011) and IV (Soszyński et al. 2015, 2016) data to exclude Cepheids, RR Lyrae stars, and Long Period Variables from our sample because their corresponding ESO SAF spectra will also include a variation due to the intrinsic stellar pulsation velocity which is difficult to disentangle with single-epoch spectra. The exclusion of variable stars was performed using the Tool for Operations on Catalogues And Tables (TOPCAT)⁵ and a maximum cross-matching distance of 1 arcsec. In total, 30 668 variable sources were removed from our sample.

⁵<http://www.star.bris.ac.uk/mbt/topcat/>

The resulting photometric data set contained 1504 220 sources. Their colour–magnitude diagram and spatial distribution are displayed in Fig. 1.

2.2 Spectroscopic data

We initially selected from the ESO SAF all objects with 1D spectra within a 10 deg radius from the SMC optical centre. The query form offers access to various parameters and the most relevant to us are outlined in Table 1. The ARCFILE (column 1) represents the name under which the data product is stored in the ESO SAF where the timestamp (ADP.timestamp) specifies the time of the data archival. The coordinates RA and Dec. (columns 2 and 3) are given in the FK5 J2000 coordinate system which are equivalent to equatorial coordinates and coordinates in the International Celestial Reference System (ICRS); the instrument and spectral grating used

Table 1. Parameters of the spectra used in this study. The table is published in its entirety as supporting material with the electronic version of the article.

ARCFILE	RA (deg)	Dec (deg)	Instrument (nm)	Grating	λ	R	SNR	Program ID	Product version
ADP.2015-04-13T10:11:06.923	13.713166	-72.637166	GIRAFFE	LR3	450–508	7500	15.8	386.D-0541	1
ADP.2015-04-13T10:11:07.283	13.797333	-72.285638	GIRAFFE	LR3	450–508	7500	60.6	386.D-0541	1
ADP.2015-04-13T10:11:13.337	14.055874	-72.652472	GIRAFFE	LR3	450–508	7500	42.2	386.D-0541	1
ADP.2015-04-13T10:11:16.837	14.412333	-72.511472	GIRAFFE	LR3	450–508	7500	12.9	386.D-0541	1
ADP.2015-04-13T10:11:26.400	13.348958	-72.481388	GIRAFFE	LR3	450–508	7500	29.7	386.D-0541	1
ADP.2015-04-13T10:11:53.937	13.948374	-72.658611	GIRAFFE	LR3	450–508	7500	138.0	386.D-0541	1
ADP.2015-04-13T10:12:02.720	13.237999	-72.484055	GIRAFFE	LR3	450–508	7500	74.8	386.D-0541	1
ADP.2015-04-13T10:12:15.860	14.158791	-72.609666	GIRAFFE	LR3	450–508	7500	112.0	386.D-0541	1
ADP.2015-04-13T10:12:19.657	13.607041	-72.393305	GIRAFFE	LR3	450–508	7500	110.4	386.D-0541	1

for the observations (columns 4 and 5) are also indicated. Column 6 represents the wavelength coverage λ , column 7, the resolving power R ($\lambda/\Delta\lambda$), and column 8, the median SNR of the spectra. Columns 9 and 10 show the Programme ID associated with the spectra and the observing date on which the spectra were obtained, respectively. Column 11 contains the product version. For single observing blocks where more than just one exposure is available, the individual spectra are stacked and are referred to as product version 2. However, this is only available for science spectra with identical instrument set-ups belonging to the same observing block. Otherwise, single spectra are referred to as product version 1.

In order to find photometric counterparts for the selected spectra, we used TOPCAT and a maximum cross-matching distance of 1 arcsec (Fig. 2). The cross-match was done using ICRS coordinates at the J2000 epoch. For each row in the spectroscopic catalogue, only the best (nearest) match from the photometric catalogue will appear as a result, but rows from the photometric catalogue may appear multiple times. This allowed us to group data by their source identifier (source ID) and identify objects with more than one spectrum. Not every object of the spectroscopic catalogue had a match in the photometric catalogue because MW stars and variable stars were excluded from our photometric catalogue using the selection criteria described in Section 2.1. We found a photometric counterpart for 24 609 spectra.

As stars can have multiple observations, we decided to use only the best spectrum of each star in terms of R and SNR. The first step was to group data by source ID and identify sources with more than one spectrum. We then proceeded to select spectra from each data group with the highest value of R ; at this stage there can still be multiple spectra as more than one spectrum can have the same R . From this list of high resolution spectra, we proceeded to select spectra with the highest value of SNR, which can also result in multiple spectra. We found that only 22 sources still have multiple spectra and we proceeded to pick a random spectrum from among those available. Furthermore, we applied one last positional cut to discard spectra belonging to the MW globular clusters 47 Tuc and NGC 362. We masked two areas centred at ($\Delta RA = 2.1$ deg, $\Delta Dec. = 0.6$ deg) and ($\Delta RA = -0.9$ deg, $\Delta Dec. = 1.96$ deg) with radii of 0.22 and 0.17 deg, respectively. Finally, we selected only spectra with $SNR \geq 10$. After applying these selection criteria, we obtain a sample comprised of 3814 spectra, of which about 97 per cent (3700) refer to observations with the GIRAFFE spectrograph of the Fibre Large Array Multi Element Spectrograph (FLAMES). We decided to focus only on this sample because the remaining 114 spectra were obtained with other instruments and are insufficient to quantify possible systematic uncertainties. The GIRAFFE spectra in our sample have not been associated with journal publications as is visible in the ESO SAF. However, during the revision of our work,

an analysis of 206 RGB stars members of the SMC appeared in Mucciarelli et al. (2023). The distribution of the 3700 sources on the colour–magnitude diagram and across the SMC is shown in Fig. 1.

FLAMES is a multiobject spectrograph mounted on the Unit Telescope 2 (UT2; Kueyen) of the Very Large Telescope (VLT) facility at the ESO Paranal Observatory. It gives access to targets across a field-of-view of 25 arcmin in diameter and feeds two spectrographs, GIRAFFE and UVES. GIRAFFE covers the visible range, 370–950 nm, with three types of feeding fibre systems: MEDUSA, IFU, ARGUS. We limited our study to the MEDUSA mode as we are interested in 1D spectra of individual stars. In this mode, GIRAFFE provides intermediate to high resolving power (R from ~ 5000 to 38 100) spectra and can observe up to 132 targets (including sky fibres) at a given time. Each fibre has an aperture of 1.2 arcsec on the sky. The spectra obtained by GIRAFFE are cleaned from cosmic rays as a pre-processing step and consecutively have most of their instrument signature removed; they have been debiased, flat fielded, extracted, and wavelength calibrated. Their wavelength scale has been corrected to the heliocentric reference system using barycentric, heliocentric, and geocentric corrections. However, they are neither flux calibrated, nor sky subtracted. Additional information about the spectra is available in the ESO Phase 3 Data Release Description document⁶

Fig. 2 shows the parameter ranges of the spectra used in our study. The spectra have R from 6500 to 38 000, with 68 per cent having $R \leq 10 000$ and the SNR ranges from 10 to 200, with 75 per cent of the spectra having an $SNR \leq 50$. Most of the spectra were obtained during the years 2003, 2010, and 2019. The distance between photometric and spectroscopic counterparts ranges from 0 to 1 arcsec with 61 per cent of the sources having a distance ≤ 0.02 arcsec. Fig. 3 shows the distribution of the sources in PM space. Most of the sources with available spectra in the ESO SAF (black points) are within the main stellar locus of the SMC, which is outlined by a white ellipse. The photometric properties of the 3700 sources such as the NIR survey of provenance, their NIR magnitudes in the J and K_s bands, their optical magnitudes in the G , G_{BP} , and G_{RP} bands, as well as the respective photometric uncertainties are given in Table 2.

3 ANALYSIS

After applying the selection criteria outlined in the previous section and obtaining a final sample of 3700 sources, we proceed to analyse the spectra by initially performing the sky subtraction followed by full spectrum fitting to obtain line-of-sight velocities.

⁶<https://www.eso.org/rm/api/v1/public/releaseDescriptions/73>

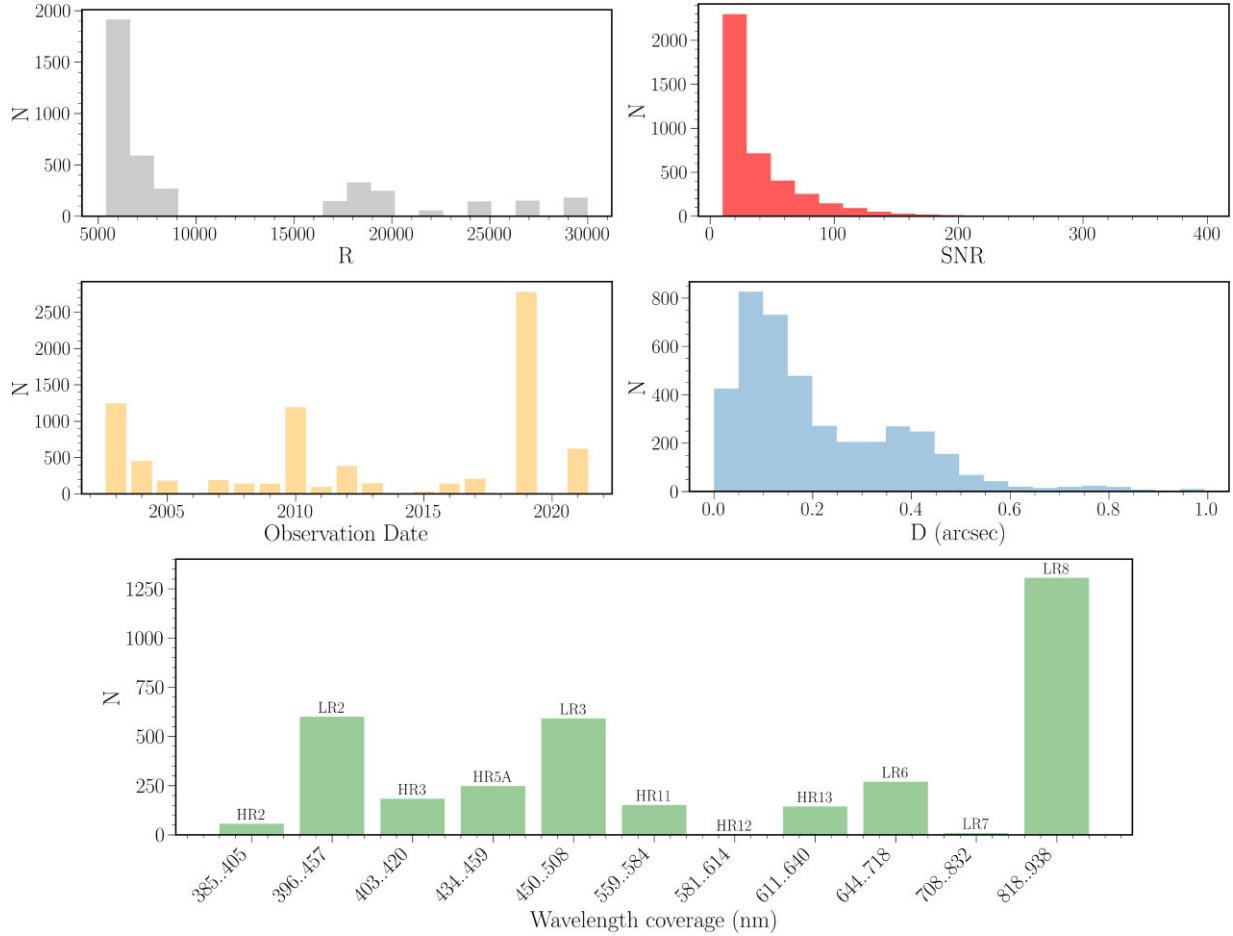


Figure 2. Histograms showing the parameter range of the spectra used in this study in terms of resolving power R (top-left), signal-to-noise ratio SNR (top-right), year of observation (middle-left), the separation between the coordinates of the photometric and spectroscopic data (middle-right), and the wavelength coverage (bottom).

3.1 Sky subtraction

The ESO pipeline recipes for GIRAFFE do not perform any sky subtraction, therefore reduced GIRAFFE spectra obtained as ESO phase 3 data products still have their sky signatures. However, when available, all fibres with a sky signal (as defined by the observer) are collected in the associated MOSSKY ancillary product files, allowing for optimal sky subtraction. Usually 10 to 20 sky fibres are assigned by the observer to obtain sky spectra. We proceed to obtain a median sky spectrum for each observing block, comprising the observation of many targets within a given plate configuration, by median combining the sky spectra available at the MOSSKY ancillary product files. Since the object spectra are already shifted to the heliocentric RV system, while the sky spectra are not, we correct the median sky spectra to the heliocentric rest frame that has been applied to the science spectra by using the header keyword HELICORR. The corrected wavelength is defined by $\lambda_{\text{cor}} = (1 + v_{\text{helio}}/c) \times \lambda_{\text{uncor}}$ with c being the speed of light and v_{helio} the projected heliocentric velocity shift that was calculated from the ESO pipeline for each science spectrum. We follow a similar methodology for the sky subtraction as in Koch et al. (2007), where the sky spectrum is modelled as a second-order Legendre polynomial plus the median sky. Additionally, we allow a small velocity shift in the sky spectrum so it is wavelength calibrated to our science spectra. We employed a Markov Chain Monte Carlo (MCMC) approach to determine the

three parameters of the second order Legendre polynomial and the small additional velocity correction using the logarithmic likelihood function given as

$$\log \mathcal{L} = \sum_{i=1}^N \left[\log \left(\frac{1}{\sqrt{2\pi}\sigma} \right) - \frac{(F_{\text{obj}} - F_{\text{sky},i})^2}{2\sigma^2} \right] \quad (1)$$

N is the number of tracers, F_{obj} is the flux of the object spectrum and $F_{\text{sky},i}$ is the modelled sky spectrum defined as the median sky in addition to the second order polynomial

$$F_{\text{sky},i} = a\lambda^2 + b\lambda + c + F_{\text{median sky}} \quad (2)$$

where a , b , and c are the parameters to be determined. The uncertainty σ results from the uncertainties on the flux of the object and sky spectra as:

$$\sigma^2 = \sigma_{\text{obj}}^2 + \sigma_{\text{median sky},i}^2 \quad (3)$$

3.2 pPXF method

In order to determine line-of-sight velocities, we are performing a full spectrum fitting using the penalized pixel fitting routine (pPXF; Cappellari & Emsellem 2004; Cappellari 2017). pPXF fits an observed spectrum with a best-fitting linear combination of differently weighted stellar templates in pixel space. It recovers the line-of-sight velocity distribution through moments of a Gauss–Hermite

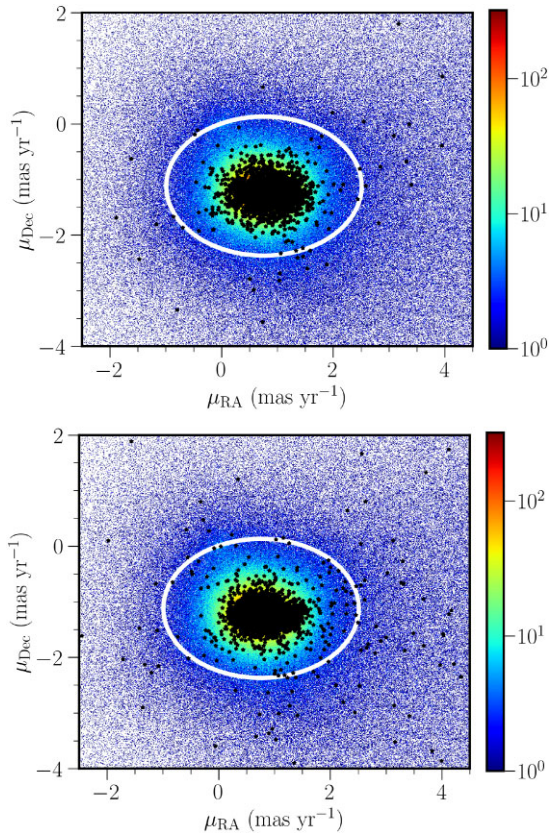


Figure 3. Stellar density of objects up to 10 deg from the SMC centre in proper motion space. The colour bars represent the number of stars. The ellipse encloses a region dominated by SMC stars. The black points show objects with available spectra in our sample (top) and in the literature sample (bottom).

series and the parameters of the distribution are optimized by a χ^2 minimization by direct comparison with the observed spectrum. The main advantage of pPXF is that it makes optimal usage of the entire spectrum, rather than focusing on a few spectral lines. pPXF has been extensively used to study kinematics of galaxies (e.g. Boardman et al. 2017); however, its implementation is independent of the system in question. The main improvement introduced in Cappellari (2017) resulted in accurate velocities regardless of the velocity dispersion σ , which in our case is simply the instrumental broadening of the spectra. The pPXF method approximates the observed spectrum using the following parametrization:

$$G_{\text{mod}}(x) = \sum_{n=1}^N w_n \left\{ [T_n(x) * \mathcal{R}_n(x)] \sum_{k=1}^K a_k \mathcal{P}_k(x) \right\} + \sum_{l=0}^L b_l \mathcal{P}_l(x),$$

where \mathcal{R}_n are the line-of-sight velocity distributions, $T_n(x)$ represent the templates, $\mathcal{P}_k(x)$ and $\mathcal{P}_l(x)$ are multiplicative and additive orthogonal polynomials of degrees k and l , respectively, while w_n , a_k , and b_l are weights to be solved for. The implementation of pPXF requires several inputs including a set of spectral templates. The noise spectrum of the observations and the starting value for the velocity and line broadening are also required. The input and noise spectra of the object to be measured are normalized and logarithmically rebinned while conserving the flux, using the `log_rebin` routine from pPXF.

Even after performing the sky subtraction, some of our spectra still suffer from contamination of sky emission lines and residual

bad pixels, which can affect the fit severely. In order to further clean our spectra, we use the following methodology. We median smooth the log rebinned spectrum by 7 pixels and then subtract the smoothed spectrum from the not-smoothed spectrum. Using this residual-subtracted spectrum, we proceed to use an iterative sigma clipping that selects all pixels that deviate from the mean by more than 3σ ; the clipping is iterative until convergence is achieved (i.e. until no pixels are removed). We then expand the binning mask by ± 2 pixels, we obtain the indices of the good pixels and feed them to pPXF by using the `goodpixels` keyword; only these spectral pixels are included in the fit.

The pPXF method combines the set of input template spectra to best-fitting the observed spectrum. These templates can either be synthetic or empirical. Considering the resolving power and wavelength range of our spectra (Fig. 2), we chose the X-shooter Spectral Library (XSL; Arentsen et al. 2019; Gonneau et al. 2020). This library contains empirical spectra with a resolving power close to $R = 10\,000$ for stars across a large range of spectral types and chemical compositions, which account for the different stellar populations we have in our sample. The spectra cover the following ranges of stellar parameters: $2\,600 \leq T_{\text{eff}} \leq 38\,000$ K, $0.0 \leq \log(g) \leq 5.7$, and $-2.5 \leq [\text{Fe}/\text{H}] \leq +1.0$ dex. They are corrected for RV and provided in the rest frame (with wavelength in air) logarithmically sampled in wavelength and normalized.

The full spectrum fit is conducted using fourth order additive and multiplicative Legendre polynomials in order to account and correct for any potential low-frequency differences in shape between the target's and the template's spectra continuum shape. Since pPXF uses a local minimization algorithm, reasonably close starting values (V_{start}) of the velocity and line broadening are required in order to avoid the algorithm to converge prematurely and hence being stuck in a local minimum. For V_{start} values ranging from 0 to 200 km s^{-1} with a step of 25 km s^{-1} are used; as to the line broadening, since we are dealing with stellar spectra, we set the starting value as the quadratic difference between the stellar spectra and templates' instrumental resolutions. We resample the stellar spectra and their associated uncertainties onto the arbitrary wavelength grid of the templates, while preserving the integrated flux. In order to evaluate whether the results represent a good fit, a reduced χ^2 as close as possible to 1 should be returned; furthermore, we visually inspect the fit. We assess any potential template mismatch by analysing the residual of the fit where the standard deviation of the residuals should be similar to their mean, for a good template match. Note that, pPXF assigns a linear combination of templates to each source (usually between 6 and 10) so there is no single template star corresponding to each source. In addition, our templates are not set on a regular grid and since we did not apply regularization of the fits they are not expected to cluster around specific parameter values. In the appendix, we show two examples. This work is focused on determining line-of-sight velocities whereas stellar parameters (temperature, surface gravity, and metallicity) will be explored in a subsequent study.

3.3 Systematic uncertainties

To evaluate the systematic uncertainties that might arise from the use of different GIRAFFE gratings, we obtain RVs for objects that have an available spectrum in at least two gratings. We found that these spectra always belong to the same Programme ID. Table 3 outlines the number of objects in common between these gratings. As it appears in the table, this is only available for eight combinations of gratings. These spectra have undergone the same analysis discussed in Sections 3.1 and 3.2. Fig. 4 shows the comparison between the

Table 2. Photometric characteristics of the spectra. The table is published in its entirety as supporting material with the electronic version of the article.

NIR source ID	NIR survey	<i>Gaia</i> EDR3 source ID	<i>G</i> (mag)	σ_G^a (mag)	\bar{G}_{BP} (mag)	$\sigma_{G_{BP}}^a$ (mag)	\bar{G}_{RP} (mag)	$\sigma_{G_{RP}}^a$ (mag)	<i>J</i> (mag)	σ_J (mag)	<i>K_s</i> (mag)	σ_{K_s} (mag)
558358499858	VMC	4 688 987 114 793 104 384	18.665	0.003	18.477	0.015	18.640	0.036	18.775	0.038	18.799	0.072
558370021706	VMC	4 689 011 166 567 250 944	15.344	0.003	15.283	0.006	15.429	0.006	15.408	0.004	15.145	0.007
558358869977	VMC	4 685 986 066 534 948 864	15.755	0.003	15.661	0.004	15.883	0.005	16.099	0.006	16.297	0.012
558370088420	VMC	4 688 995 498 568 136 704	19.036	0.004	18.696	0.039	18.715	0.051	18.675	0.027	18.466	0.082
558369977606	VMC	4 689 004 986 121 150 464	17.156	0.005	16.922	0.006	17.106	0.008	17.274	0.011	17.369	0.034
558358846869	VMC	4 685 985 933 366 169 600	13.271	0.003	13.289	0.003	13.207	0.004	13.158	0.001	13.108	0.003
558369967505	VMC	4 689 005 054 840 926 208	14.645	0.004	14.648	0.021	14.602	0.028	14.615	0.003	14.561	0.006
558358892671	VMC	4 685 986 483 121 884 160	13.567	0.003	13.511	0.003	13.661	0.004	13.828	0.002	13.865	0.004
558370002756	VMC	4 689 007 322 583 053 312	13.844	0.003	13.794	0.003	13.883	0.005	13.988	0.002	13.956	0.004

^aThe standard error of *G*, \bar{G}_{BP} , and \bar{G}_{RP} mean magnitudes were computed as a simple error propagation on the fluxes, according to the formula: $\sigma_G = \sqrt{(-2.5/\ln(10) * \sigma_{F_G}/F_G)^2 + \sigma_{G_0}^2}$, where F_G is the mean flux in the *G*, \bar{G}_{BP} , or \bar{G}_{RP} bands, respectively, σ_{F_G} is the error on the mean flux, while σ_{G_0} is the zero point uncertainty.

Table 3. Number of sources observed in different GIRAFFE gratings.

	HR2	LR2	HR3	HR5A	LR3	HR11	HR13	LR6
HR2	66	0	66	64	0	0	0	0
LR2	0	600	0	27	100	0	0	83
HR3	66	0	183	69	0	0	0	0
HR5A	64	27	69	248	17	0	0	0
LR3	0	100	0	17	591	0	0	83
HR11	0	0	0	0	0	152	11	0
HR13	0	0	0	0	0	11	144	0
LR6	0	83	0	0	83	0	0	270

RV estimates where the mean difference in terms of velocity and the respective standard deviation is indicated. We find mean differences in velocities of $1.77 \pm 0.22 \text{ km s}^{-1}$. The dispersion within each grating is about 1 km s^{-1} . These differences might be related to the non-uniform fibre illumination, the template mismatch in the cross-correlation procedure, as well as the resolution and SNR of the spectra. As they could not be estimated for enough combinations of gratings to homogenize the sample, we refrain from applying a correction for the systematic uncertainties.

4 RESULTS

4.1 Radial velocities

Fig. 5 displays the distribution of RVs derived for the 3700 sources in the ESO SAF sample. It shows two distinct peaks with a small peak around $18 \pm 2 \text{ km s}^{-1}$ representing the MW foreground stars in the direction of the SMC and a large peak around $159 \pm 2 \text{ km s}^{-1}$ representing stars belonging to the SMC. The latter corresponds to a velocity dispersion (σ_V) of $33 \pm 2 \text{ km s}^{-1}$ which is the best-fitting sigma of the Gaussian without taking into account the velocity errors. The limits to the tails of the RV distribution representing SMC stars are set at 60 and 258 km s^{-1} which is $\pm 3\sigma_V$ of the distribution. The measured velocities and their corresponding uncertainties are summarized in Table 4. In this table, we indicate also the velocities corrected for the projected bulk proper motion, the values of the correction, the initial velocity used by the pPXF routine (V_{start}), the reduced χ^2 , the formal velocity error (V_{error}) and the corrected velocity error ($V_{\text{error}} \times \chi^2$). Formal uncertainties provided directly by pPXF are based on the covariance matrix of the fitted parameters under the assumptions that the χ^2 space is smooth, unimodal and close to unity. These errors only serve as an estimate of the order

of magnitude unless $\chi^2 \sim 1$. We find that 92 and 99 per cent of our sample has a $V_{\text{error}} \leq 5 \text{ km s}^{-1}$ and $V_{\text{error}} \leq 10 \text{ km s}^{-1}$, respectively. Our mean RV is $\sim 10 \text{ km s}^{-1}$ higher compared to other studies such as De Leo et al. (2020) and Dobbie et al. (2014) where the mean of their distributions was found to be around 149 km s^{-1} . This difference is due to combining different type stellar populations. De Leo et al. (2020) and Dobbie et al. (2014) observed giant stars while the mean in our study also includes main-sequence and supergiant stars. The overall distribution of RVs derived in literature studies is also shown in Fig. 5 and discussed in Section 4.2. The RV of the different stellar populations in this work is further explored in Section 4.3.1.

4.2 Radial velocities from the literature

Several spectroscopic studies have targeted the SMC using different stellar populations to characterize its internal kinematics. In our analysis, we consider data from the following literature studies and construct a comprehensive homogenized catalogue to complement the spectroscopic sample obtained in Section 2.2.

(i) Carrera et al. (2008) presented the chemical enrichment of the SMC by providing stellar metallicities as well as RVs for 350 RGB stars distributed across the inner 4 deg of the galaxy. The observations were carried out using the visual and near-ultraviolet FOcal Reducer and low dispersion Spectrograph 2 (FOR2) at the VLT in 13 fields of about $7 \times 7 \text{ arcmin}^2$ each in size. The Spectroscopic Mask (MXU) mode was used to obtain multi-object spectra in the wavelength range 773–948 nm with $R = 2560$. This study outlined the first spectroscopic metallicity gradient in the SMC and RVs were also used to reject non-SMC members from the sample. Their RV uncertainty was $\sim 4 \text{ km s}^{-1}$.

(ii) Evans & Howarth (2008) traced the dynamics of the young stellar population of the SMC by obtaining RVs of 2045 OBA-type stars. They observed with the Two Degree Field Facility (2dF) at the Anglo-Australian Telescope (AAT) and obtained spectra that cover the wavelength range 390–480 nm. The resolving power of $R = 1600$ resulted in an accuracy of $\sim 11 \text{ km s}^{-1}$ on the RV of individual stars distributed across an area of $2 \times 12.5 \text{ deg}^2$. The authors found a velocity gradient across the SMC bar of $26.3 \pm 1.6 \text{ km s}^{-1} \text{ deg}^{-1}$ at PA = 126 deg. They also noted a difference in RV between the Wing and bar as well as a $\sim 20 \text{ km s}^{-1}$ red-shift of their young stars compared to older stellar populations.

(iii) Harris & Zaritsky (2006) observed 2046 red giant stars in the central $4 \times 2 \text{ kpc}^2$ of the galaxy using the Inamori-Magellan Areal Camera and Spectrograph (IMACS) at the Magellan Baade

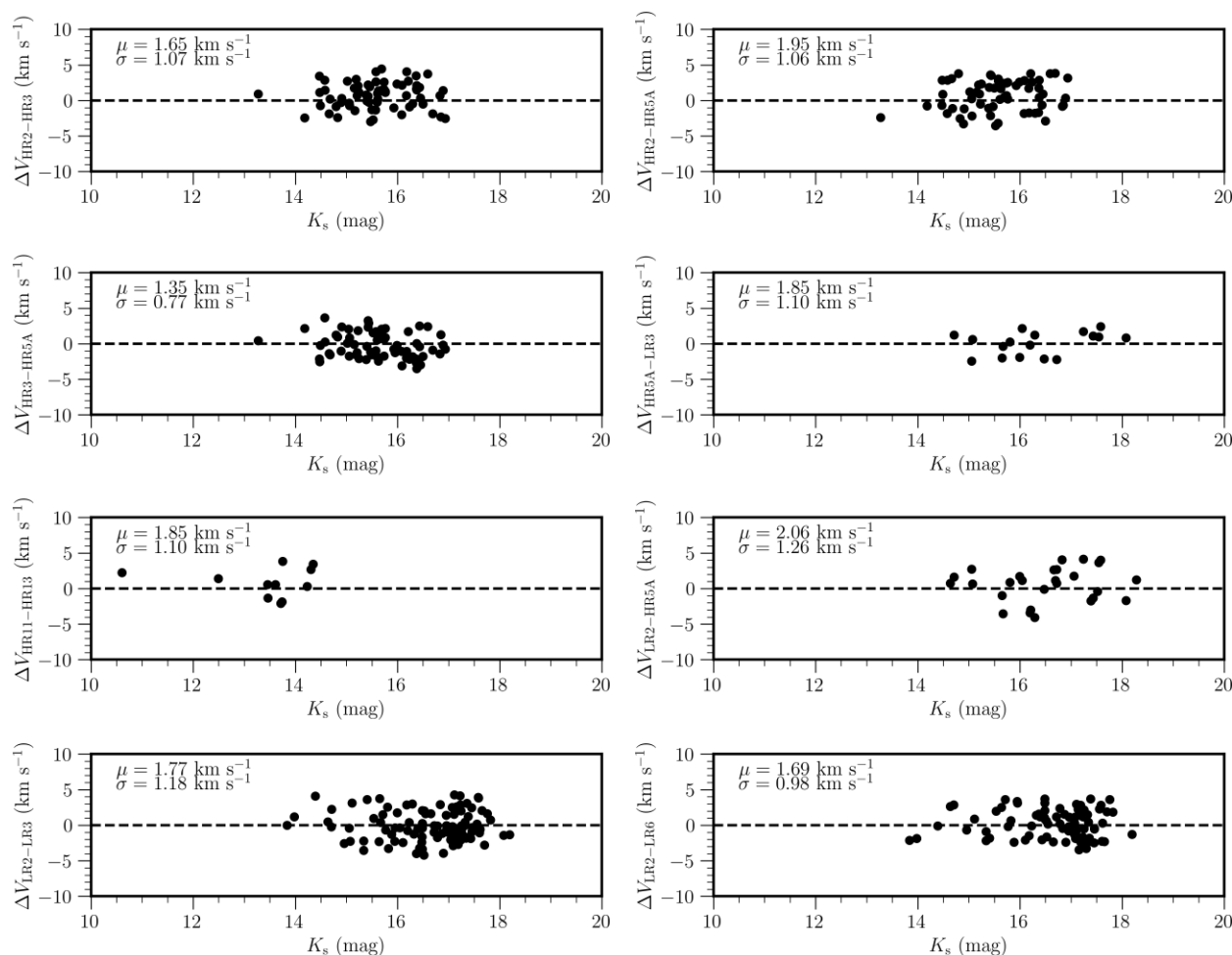


Figure 4. Comparison between the RVs estimated from spectra obtained with different GIRAFFE gratings as a function of magnitude. Means and corresponding standard deviations are indicated within each panel. The uncertainty on individual points corresponds to 2 km s^{-1} .

Telescope. The spectra spanned a wavelength range from 560–1000 nm with a resolving power $R \sim 5000$ resulting in a RV uncertainty of $\approx 10 \text{ km s}^{-1}$. The authors found a global velocity distribution centred at 146 km s^{-1} with a dispersion of 28 km s^{-1} as well as evidence of a velocity gradient across the SMC.

(iv) Dobbie et al. (2014) provided RVs of 4172 red giant stars and 352 carbon stars across an area of 37.5 deg^2 with an accuracy better than 5 km s^{-1} . The spectra were acquired using the AAOmega spectrograph at the AAT. The blue and red arms of the instrument were configured with the 1500V ($R \sim 4000$) and 1700D ($R \sim 10\,000$) gratings with a wavelength coverage ranging from 425–600 nm and 845–900 nm, respectively. The authors found that a rotating disc model best represents the rest-frame velocity of the youngest red giants in their sample. Beyond $\geq 4 \text{ deg}$, they found signatures of tidal stripping. Their global velocity distribution is centred at $147.8 \pm 0.5 \text{ km s}^{-1}$.

(v) Lamb et al. (2016) observed 374 stars as part of the RIOTS4 Survey, a uniformly selected survey of young stars in the SMC. They found that the SMC has a systemic velocity of $\sim 150 \text{ km s}^{-1}$ and kinematics like those of other massive stars surveys (e.g. Evans & Howarth 2008). Their spectral coverage for each star varied. However every spectrum includes the wavelength range from 400–470 nm. A majority of their targets (328) were observed using IMACS at the Magellan Baade telescope with a spectral resolving power of

$R = 2600\text{--}3700$. The other targets were observed with IMACS at a resolving power of $R = 1000\text{--}1300$ or with the Magellan Inamori Kyocera Echelle (MIKE) Spectrograph on the Magellan Clay telescope with a resolving power of $R \sim 28\,000$. The uncertainties on their RV measurements are $\sim 5 \text{ km s}^{-1}$ for MIKE observations and $10\text{--}25 \text{ km s}^{-1}$ for IMACS observations.

(vi) De Leo et al. (2020) targeted 2573 red giant stars within $\sim 4 \text{ kpc}$ from the SMC’s centre using the AAOmega spectrograph at the AAT. Observations used the grating 1700D spanning a wavelength coverage of 845–900 nm and providing a resolving power of $R \sim 8500$. They achieved a velocity uncertainty better than 5 km s^{-1} and their velocity distribution is centred at $\sim 150 \text{ km s}^{-1}$. They found an outward stellar motion in the direction towards the LMC supporting that the SMC is undergoing tidal disruption.

(vii) Nidever et al. (2020) studied 3800 objects in the Magellanic Clouds using data from the Sloan Digital Sky Survey (SDSS) DR16 (Ahumada et al. 2020). Observations were obtained from the Apache Point Observatory Galactic Evolution Experiment 2 South (APOGEE-2S; Majewski et al. 2017; Wilson et al. 2019) on the du Pont telescope at Las Campanas Observatory (LCO) in the near-infrared (1.51–1.70 μm) with a resolving power of $R \sim 20\,000$. Nidever et al. (2020) mostly focused on the RGB population, but observations included also asymptotic giant branch (AGB) stars, main-sequence stars, and supergiants distributed within 10 deg of

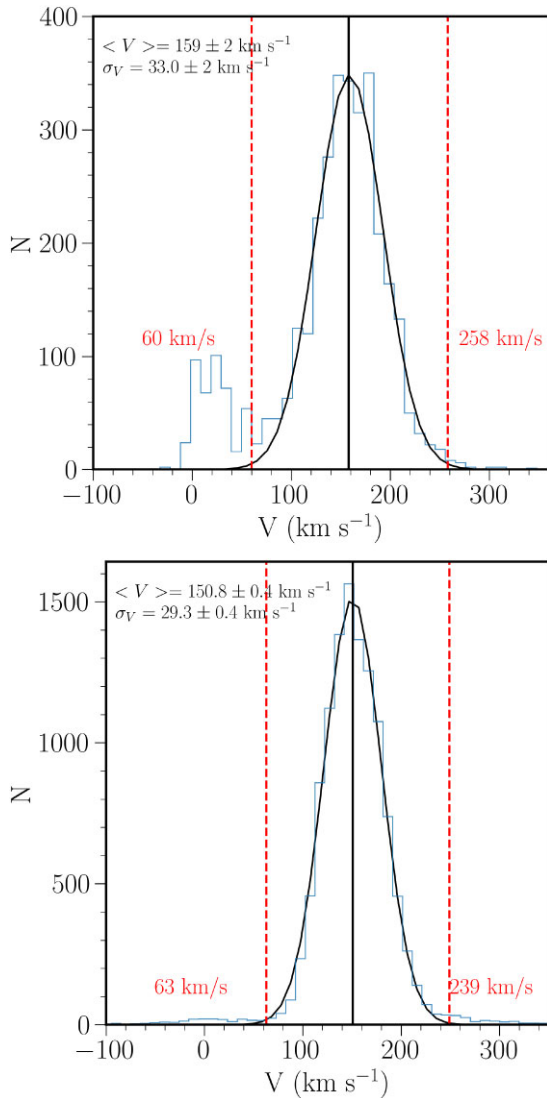


Figure 5. Distribution of RVs from our sample (top) and the homogenized literature (bottom). Black continuous lines represent the Gaussian fit of the distribution for SMC stars and the corresponding mean. The latter and its dispersion are indicated at the top left. The bin size is 10 km s^{-1} . Red vertical dashed lines mark the velocity cuts applied to reduce the influence of MW stars. These are also indicated on each side of the lines.

the LMC and 6 deg of the SMC centres. They obtained a mean radial velocity of 135 km s^{-1} and RV uncertainties of $\sim 0.1\text{--}0.2 \text{ km s}^{-1}$. In our study, we use the current DR17 (Abdurro’uf et al. 2022) which contains observations for 3600 objects in the SMC.

(viii) *Gaia* DR3 (Gaia Collaboration et al. 2022) contains median RVs for 33 812 183 stars brighter than $G = 14$ mag and distributed throughout the entire celestial sphere. The median formal precision of the RVs is of 1.3 km s^{-1} at $G = 12$ mag and 6.4 km s^{-1} at $G = 14$ mag (Katz et al. 2022). The spectra are taken with the Radial Velocity Spectrograph and have a resolving power of $R \sim 11500$ across a wavelength range of 845–872 nm.

We proceed to cross-match the targets of the literature studies with our photometric sample outlined in Section 2.1 to obtain their NIR photometry and *Gaia* EDR3 astrometric solution. The cross-matching facility of TOPCAT were used adopting a maximum cross-matching distance of 1 arcsec. Fig. 1 shows the NIR CMD of the

sources in the literature sample and their location across the different stellar population regions outlined in El Youssoufi et al. (2019) as well as their spatial distribution, which displays the coverage of the main body of the galaxy and of some fields in the outskirts. The location of the fields studied by Cullinane et al. (2023) using data from the Magellanic Edges Survey is also indicated. Fig. 3 shows the distribution of the sources across the PM space highlighting that most of them are enclosed within a region containing a reduced number of MW stars due to the astrometric selection criteria discussed in Section 2.1.

We then cross-match the targets among the literature studies to find common sources. Their numbers are summarized in Table 5. As a consequence of combining data from different spectroscopic literature studies, we need to assess if there are any systematic offsets present in the RVs and to take them into account to produce a homogenized sample. We decided to anchor the RVs on APOGEE DR17. This catalogue has data with the highest resolving power, which span different stellar populations, and has sources in common with almost all of the other studies. Table 6 summarizes the number of objects each study has in common with APOGEE DR17 and provides the median differences between the RVs ($\langle \Delta V \rangle$) of APOGEE DR17 and the other studies as well as the standard deviation of the differences ($\sigma_{\Delta V}$). We eliminate duplicates by retaining sources with the most precise RVs and obtain a homogeneous sample by adding the median RV differences to each study respectively (for example, $V = V_{\text{Dobbie et al.}} + \langle \Delta V \rangle$). We discard the Carrera et al. (2008) sample because it does not have enough sources in common with APOGEE DR17 or other studies. Our final homogenized sample of RVs from the literature studies contains 9110 sources. Fig. 5 displays the distribution of RVs derived for the literature sample. It shows a single peak at $150.8 \pm 0.4 \text{ km s}^{-1}$ representing stars belonging to the SMC, with $\sigma_V = 29.3 \pm 0.4 \text{ km s}^{-1}$. The tails of the RV distribution representing SMC stars are set at 63 and 239 km s^{-1} which is $\pm 3\sigma_V$ of the distribution. We find that the velocity dispersion between the ESO SAF and literature samples agree within their dispersions. However the mean velocities differ by $\sim 8 \text{ km s}^{-1}$. A one-to-one comparison of the velocities for the sources in common is shown in Fig. 6. The distribution appears flat because the data spread is similar within both ranges of RVs. The distribution of residuals, except for the few sources at the lowest and highest velocities, does not show any obvious trends overall and for any of the samples. We find a mean star by star offset of $V_{\text{ESO}} - V_{\text{Lit}} = -6.5 \text{ km s}^{-1}$ for targets in common and a velocity dispersion of 38.8 km s^{-1} , which is larger than the errors on individual sources.

4.3 Stellar kinematics of the SMC

4.3.1 Kinematics of stellar populations

Fig. 7 compares the RV distributions of different CMD regions (El Youssoufi et al. 2019) between our sample and the literature sample. The majority of the stars in our sample populate region A (main-sequence stars) and J (RC stars). There are also many stars (about 200 or more) in regions B (main-sequence stars), E (faint RGB stars), G, H and I (supergiant stars), and K (bright RGB stars). Very few stars are found in region M (AGB stars). In particular, our sample provides RVs for stars in regions B, E, and J which are poorly sampled in the literature studies. It is noticeable that regions E, I, and J are those mostly contaminated by MW stars which have small RVs. In the following, we consider stars with $60 < V < 258 \text{ km s}^{-1}$ to belong to the SMC and we compute mean RVs within each region by fitting a Gaussian to their RV distributions using

Table 4. RVs of sources from the 3700 sources in our sample. The table is published in its entirety as supporting material with the electronic version of the article.

ARCFILE	V km s ⁻¹	$V_{\text{corr.}}$ km s ⁻¹	corr. km s ⁻¹	V_{error} km s ⁻¹	χ^2	$V_{\text{error}} \times \chi^2$ km s ⁻¹
ADP.2015-04-13T10:11:06.923	185.1	185.6	0.5	5.8	0.5	2.9
ADP.2015-04-13T10:11:07.283	139.5	142.0	-2.5	0.9	0.8	0.7
ADP.2015-04-13T10:11:13.337	183.7	183.8	-0.1	3.8	0.3	1.1
ADP.2015-04-13T10:11:16.837	164.8	165.3	-0.5	8.7	0.4	3.5
ADP.2015-04-13T10:11:26.400	98.6	100.4	-1.8	4.0	0.4	1.6
ADP.2015-04-13T10:11:53.937	152.5	152.6	-0.1	0.7	5.5	3.8
ADP.2015-04-13T10:12:02.720	173.0	174.9	-1.9	1.2	0.4	0.5
ADP.2015-04-13T10:12:15.860	165.3	165.5	-0.2	0.7	0.8	0.6
ADP.2015-04-13T10:12:19.657	181.8	183.9	-1.2	0.8	0.8	0.6

Table 5. Number of sources found in our NIR photometric sample and in common among the RV literature studies.

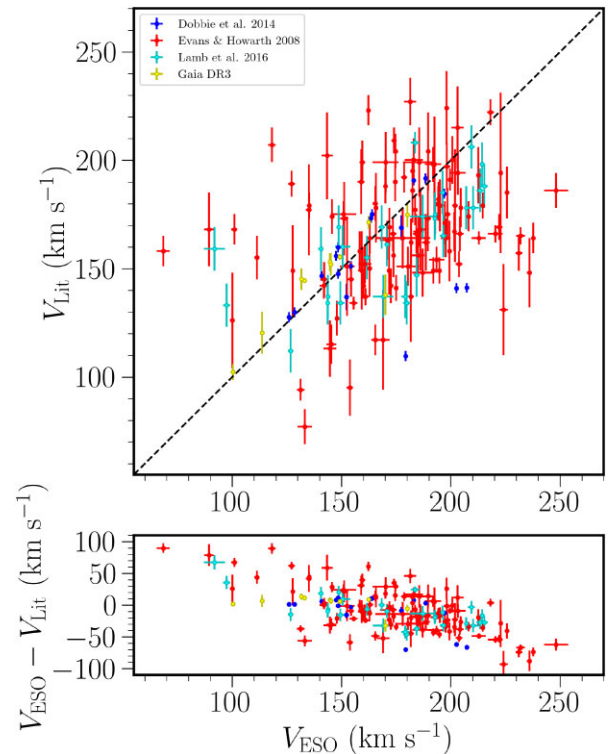
	$N_{\text{APOGEE DR17}}$	$N_{\text{Dobbie et al.}}$	$N_{\text{De Leo et al.}}$	$N_{\text{Harris \& Zaritsky}}$	$N_{\text{Evans \& Howarth}}$	$N_{\text{Carrera et al.}}$	$N_{\text{Lamb et al.}}$	$N_{\text{Gaia DR3}}$
$N_{\text{APOGEE DR17}}$	1913	103	97	0	9	0	2	115
$N_{\text{Dobbie et al.}}$	103	2743	103	93	1	2	0	180
$N_{\text{De Leo et al.}}$	97	103	1005	4	0	2	0	0
$N_{\text{Harris \& Zaritsky}}$	0	93	4	1581	0	1	0	0
$N_{\text{Evans \& Howarth}}$	9	1	0	0	1303	0	35	18
$N_{\text{Carrera et al.}}$	0	2	2	1	0	215	0	0
$N_{\text{Lamb et al.}}$	2	0	0	0	35	0	196	0
$N_{\text{Gaia DR3}}$	115	180	0	0	18	0	0	2833

Table 6. RV differences between APOGEE DR17 and literature studies.

	N	$\langle \Delta V \rangle$ km s ⁻¹	$\sigma_{\Delta V}$ km s ⁻¹
APOGEE DR17 – Dobbie et al.	103	0.51	3.51
APOGEE DR17 – De Leo et al.	96	-0.07	3.03
APOGEE DR17 – Evans & Howarth	9	-8.86	67.77
APOGEE DR17 – Carrera et al.	0	-	-
APOGEE DR17 – Lamb et al.	2	7.14	99.41
APOGEE DR17 – Gaia DR3	115	0.03	3.93
APOGEE DR17 – Harris & Zaritsky	0	1.53 ^a	18.72 ^a
Dobbie et al. – Harris & Zaritsky	93	1.10	16.10
Evans & Howarth – Lamb et al.	35	16.00	31.64

^aThis value was calculated from the combination of the results from APOGEE DR17 – Dobbie et al. and Dobbie et al. – Harris & Zaritsky samples.

a non-linear least-squares minimization technique. The number of sources in both our sample and the literature sample, the respective values of RVs and dispersions, as well as the corresponding median ages and age intervals of the stars within each CMD region are reported in Table 7. This shows that there are two groups differing by 20 km s⁻¹: one formed by stars in regions A, B, G, H, and M with a RV of ~ 170 km s⁻¹ and another one formed by stars in regions E, I, J, and K with a RV of ~ 150 km s⁻¹. The velocity dispersion of each region is comparable and corresponds to ~ 30 km s⁻¹. The same dichotomy is found for stars in the literature sample with the exception of those in region M which have instead a mean RV of ~ 150 km s⁻¹. However, in our sample regions B, J, and M contain only a few stars and it may not be appropriate to compare their mean values with those from regions that are instead well populated. Fig. 8 shows the spatial distribution of the RVs across the SMC for stars in the two samples whereas Fig. 10 shows similar distributions but for each CMD region. The literature sample, which encompasses a rather homogeneous wide area of the galaxy, shows larger RVs to the SE of the SMC centre and lower RVs in the other area along and west of the bar. A large RV to the SE is also present in our sample, but it

**Figure 6.** (top) Comparison between the RVs from our sample obtained in this study versus those derived in literature studies. The dotted line shows the one-to-one relation. (bottom) Distribution of residuals with a mean velocity of -6.5 km s⁻¹ and a velocity dispersion of 38.8 km s⁻¹.

is more difficult to discern an overall RV trend because our sample is concentrated on the bar with only sparse fields located around it. We computed the perspective correction to the RVs from the projected bulk proper motion of the galaxy (Fig. 9). We used the coordinates for

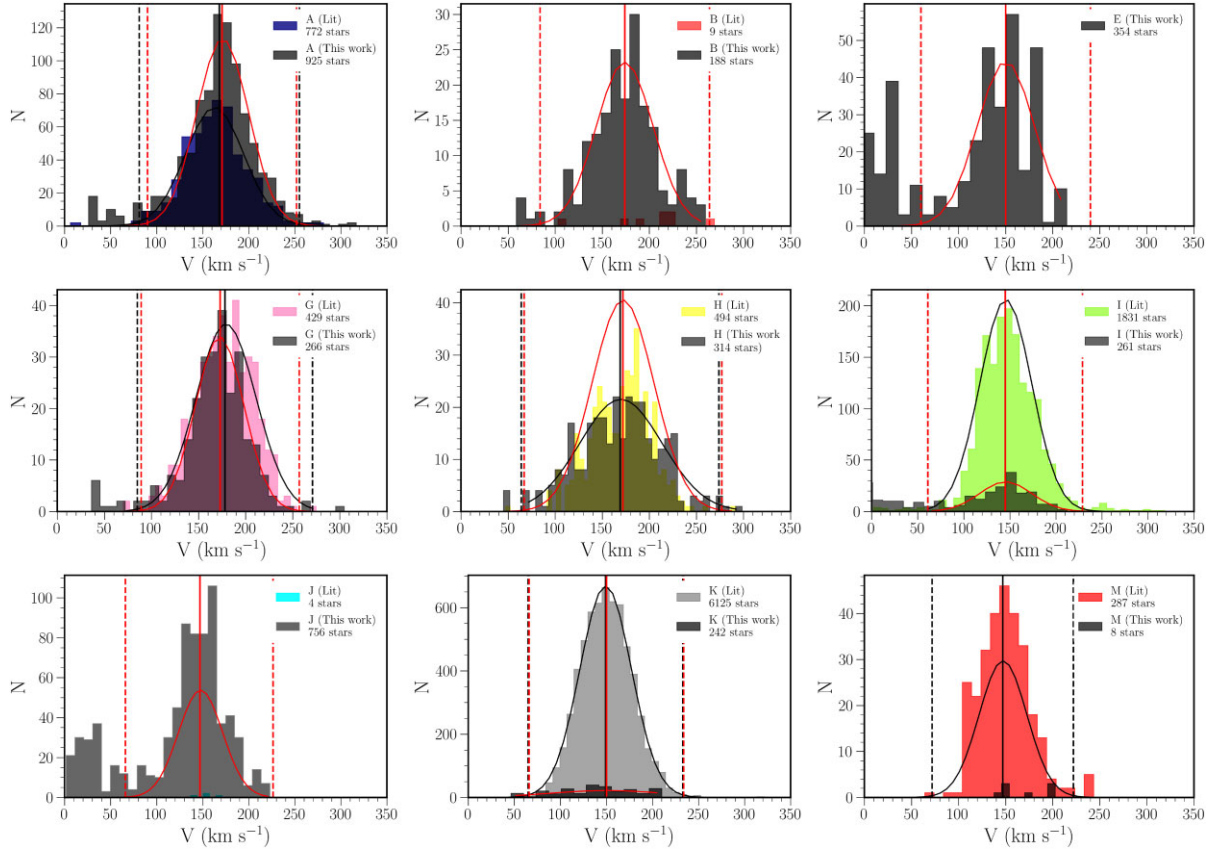


Figure 7. Distributions of RVs in the different CMD regions outlined in Fig. 1 and adapted from El Yousoufi et al. (2019), for the literature sample (coloured histograms) and our sample (dark grey histograms). The distribution of SMC stars within each panel is fitted with a Gaussian. The vertical axes represent the number counts within bins of 12 km s^{-1} in size. Regions C and D are not included due to the low number of sources.

Table 7. Mean radial velocity for each CMD region.

CMD Region	ESO SAF sample			Literature sample			Median age ^a Myr	Age range ^a Myr
	N	$\langle V \rangle$ km s^{-1}	σ_V km s^{-1}	N	$\langle V \rangle$ km s^{-1}	σ_V km s^{-1}		
A	925	171	28	772	168	30	20	10–50
B	188	174	30	9	201	38	150	50–410
C	28	32	8	–	–	–	700	250–2000
D	–	–	–	–	–	–	2500	1500–5000
E	354	150	30	–	–	–	4500	2500–8000
G	266	173	28	429	179	31	110	50–230
H	314	169	36	494	172	33	230	150–360
I	261	145	28	1831	146	28	510	90–3000
J	756	148	27	4	152	12	4000	2000–9000
K	242	151	28	6125	149	28	4000	2000–8000
M	8	170	25	287	147	25	2500	1000–5000

^aAges are from El Yousoufi et al. (2019).

the centre ($\alpha = 13.05 \text{ deg}$, $\delta = -72.03 \text{ deg}$) as given in Section 2, the proper motions ($\mu_\alpha \cos \delta = 0.686 \text{ mas yr}^{-1}$, $\mu_\delta = -1.237 \text{ mas yr}^{-1}$) from Gaia Collaboration et al. (2021b) and the distance modulus $(m-M) = 18.88 \text{ mag}$ from Muraveva et al. (2018). Fig. 9 shows that the correction on the eastern side of the galaxy is larger than on its western side suggestive of a rotation pattern, but it is constant along the bar region.

Regions A and B represent both main-sequence populations and their morphology delineates the asymmetric nature of the galaxy (El Yousoufi et al. 2019). In these regions, both samples are of a

comparable size and populate the bar and the Wing. The literature sample is also present between the two structures, but only for stars 10–50 Myr old, and our sample provides stars 50–410 Myr old (El Yousoufi et al. 2019). Regions G and H represent supergiant populations of 30–200 Myr old and 130–340 Myr old, respectively, and the two samples show similar distributions to those in regions A and B despite having about twice as many sources in the literature sample than in our sample. In contrast in region I, which is also populated by supergiant stars with a median age of ~ 510 Myr (El Yousoufi et al. 2019), we find that both samples probe the extended

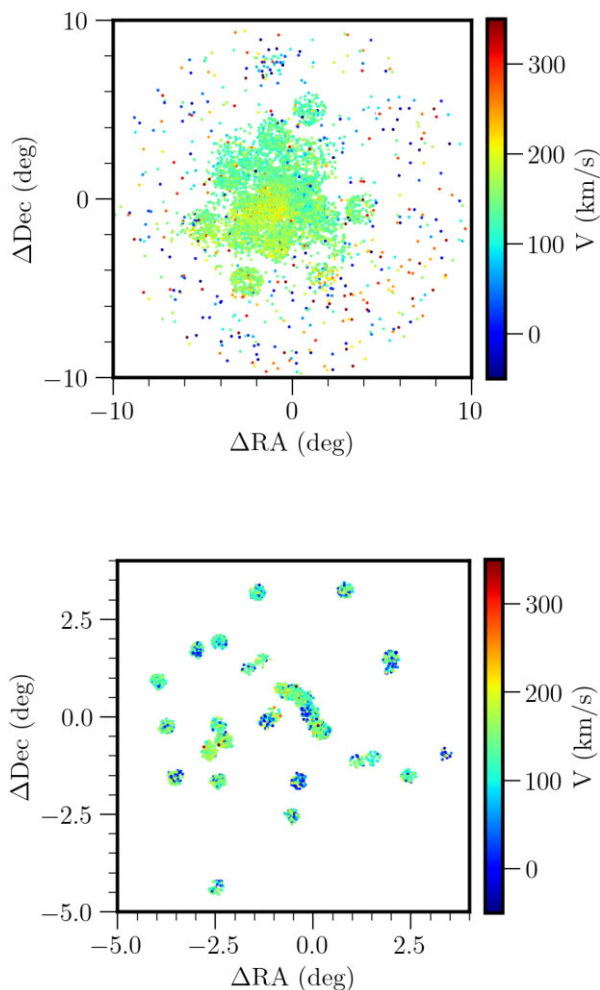


Figure 8. Distribution of RVs obtained from the literature sample (top) and our sample (bottom).

body of the galaxy. Region I includes fainter stars than those in regions G and H. The literature sample has also a large concentration of stars in the SW part of the bar compared to the part in the NE. Regions E and K represent the faint and bright RGB populations, respectively with an approximate range of 2–8 Gyr (El Youssoufi et al. 2019). Our sample in region E occupies sparse fields in the outskirts of the galaxy with more fields being present in the east than in the west. There are no stars in the literature sample from this region. Our sample in region K has a similar spatial distribution as that of region E. Region K encompasses the largest number of stars in the literature sample and the widest coverage of the galaxy. The comparison between region K and regions populated by younger stars highlights that the NE of the bar is on average younger than its SW as well as other regions around it. The RVs of the old populations are on average lower than those of the young populations. This is perhaps due to the young stars having formed out of gas already influenced by tidal stripping. Region J represents the RC population with an age in the range from 2–9 Gyr (El Youssoufi et al. 2019) for which the spatial distribution and average RV from our sample is similar to that of regions E and K; no stars in the literature sample populate this region. Region M represents the AGB population with an approximate age of 1–5 Gyr (El Youssoufi et al. 2019). The literature sample is sparsely distributed mostly across the outer region of the galaxy. Our sample only has 8 stars in this region. In addition, regions I and M show a

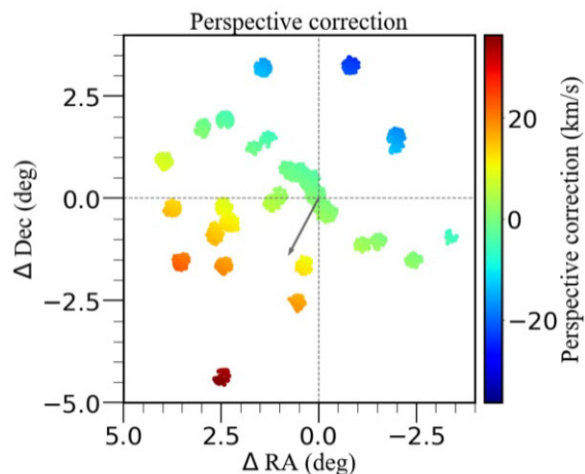


Figure 9. Distribution of the perspective correction derived from the projected bulk proper motion of the galaxy, which is indicated with an arrow departing from the centre.

small overdensity in the RV histograms around 250 km s^{-1} . However, these stars are sparsely distributed across the galaxy and do not trace a particular substructure. Due to their low number they could be fluctuations of the histogram distributions, as it appears in other CMD regions, or perhaps members of a stellar stream.

We conclude that the RVs obtained from our sample and the literature sample for stellar populations within each CMD region are in good agreement within the uncertainties. Existing differences for regions B and M can be attributed to the small size of the literature sample. We chose to proceed continuing to keep both samples separated, in order to avoid introducing systematic effects and uncertainties that may be relevant at the level of fewer sources and their spatial distribution compared to the mean values.

4.3.2 Kinematics of the bar and Wing

The distribution of sources with available RV estimates from the ESO SAF and literature samples encompasses different morphological features of the SMC. In the following, we examine the kinematics of the bar and Wing regions which are prominent features in our sample. To study the kinematics of these two regions, we define two masks to enclose them – see Fig. 11.

The SMC bar spans ~ 2.5 deg in length (El Youssoufi et al. 2019) and is also known to be elongated across the line of sight reaching up to 23 kpc (Gardiner & Noguchi 1996; Haschke, Grebel & Duffau 2012; Subramanian & Subramaniam 2012; Nidever et al. 2013; Jacyszyn-Dobrzniecka et al. 2017; Muraveva et al. 2018). The elliptical mask defined to enclose the bar is centred at ($\Delta\text{RA} = -0.35$ deg, $\Delta\text{Dec.} = 0$ deg), has a semi-minor axis of 3 deg, a semi-major axis of 1.4 deg, and a PA of 40 deg in the NE direction. We find that in the bar region, the mean RV estimates decrease by about 20 km s^{-1} with increasing stellar population age, from young main-sequence stars ($\sim 170 \text{ km s}^{-1}$) to old supergiant stars ($\sim 150 \text{ km s}^{-1}$) corresponding to an age difference of about 100 Myr. Differences in kinematics between the NE ($\Delta\text{Dec.} > 0$ deg) and SW ($\Delta\text{Dec.} < 0$ deg) bar correspond to 10 km s^{-1} in the youngest main-sequence stars, with the NE bar having the highest velocity (177 km s^{-1}). In supergiants, there is a similar velocity difference (8 km s^{-1}), but only for stars in region H (yellow supergiants) and it is the SW bar that instead has the

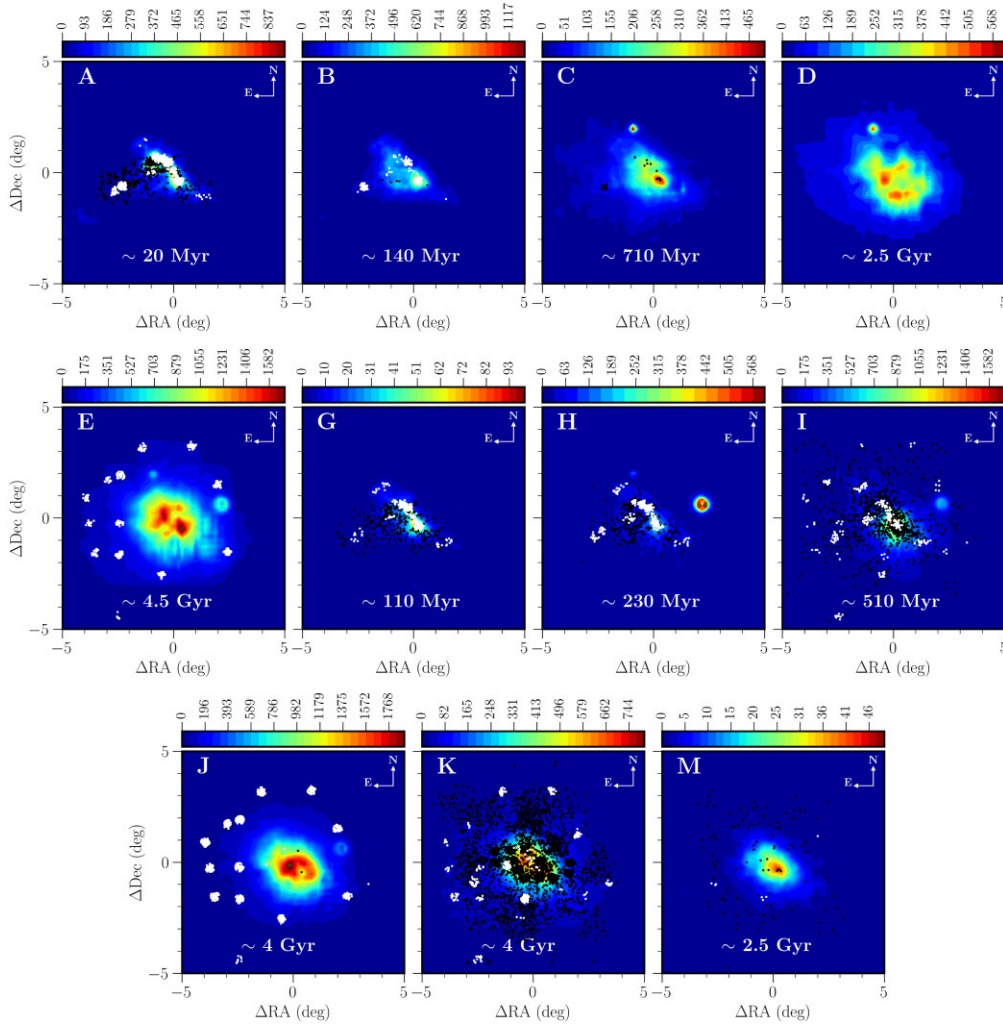


Figure 10. Distribution of RVs from our sample (white points) and the literature sample (black points) superimposed onto morphological maps of stellar populations in the SMC from El Yousoufi et al. (2019). The bin size is 0.03 deg^2 and the colour bar represents the number of stars per bin. Regions A, B, and C refer to main-sequence stars, D to main-sequence/subgiant stars, E to faint RGB stars, G, H, and I to supergiant and giant stars, J to RC stars, K to bright RGB stars, and M to thermally pulsing AGB stars. Median ages for each stellar population, as derived by El Yousoufi et al. (2019), are indicated in the panels.

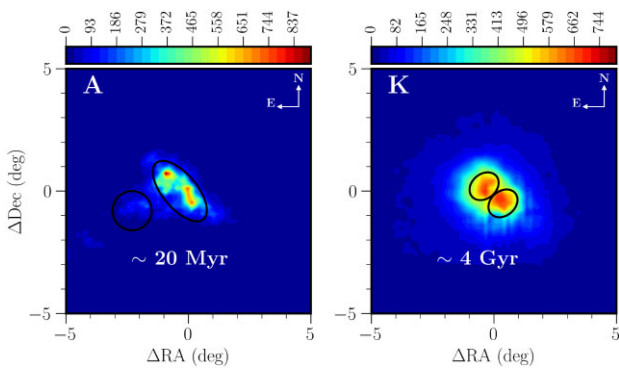


Figure 11. (Left) Morphological map of young main-sequence stars (region A) with superimposed circular and elliptical masks encompassing the Wing and bar of the SMC, respectively. (Right) Morphological map of bright RGB stars (region K) with elliptical masks encompassing two apparent overdensities. The bin size is 0.03 deg^2 and the colour bars represent the number of stars per bin. Median ages are as in Fig. 10.

highest velocity (172 km s^{-1}). Uncertainties on the RV measurements are $\sim 1 \text{ km s}^{-1}$.

At intermediate-ages, traced by bright RGB stars in region K, the inner SMC is also dominated by two overdensities which are located along the bar, but that differ in shape compared to those traced by younger stars (Fig. 11). Data for these substructures are only available in the literature sample. We calculate the mean RV of these overdensities using two masks defined as follows. The elliptical mask defined to encompass the overdensity in the NE is centred at ($\Delta\text{RA} = -0.4 \text{ deg}$, $\Delta\text{Dec} = 0.2 \text{ deg}$), has a semiminor axis of 1 deg, a semimajor axis of 1.3 deg, and a PA of 40 deg whereas the elliptical mask defined to encompass the overdensity in the SW is centred at ($\Delta\text{RA} = 0.37 \text{ deg}$, $\Delta\text{Dec} = -0.50 \text{ deg}$), has a semiminor axis of 1.0 deg, a semimajor axis of 1.3 deg, and a PA of 40 deg. Using only RVs from bright RGB stars, we obtain that the SW overdensity has a mean RV of $152 \pm 1 \text{ km s}^{-1}$ whereas the NE overdensity has a mean RV of $144 \pm 1 \text{ km s}^{-1}$. These velocities are similar to the velocity of old supergiant stars.

The Wing is a morphological substructure discovered by Shapley (1940), located at the SE of the SMC, connecting the galaxy to the

Magellanic Bridge. The circular mask defined to cover the Wing is centred at ($\Delta\text{RA} = -2.30$ deg, $\Delta\text{Dec.} = -0.80$ deg) and has a radius of 0.80 deg. We find that both the youngest main-sequence stars and supergiant stars show the same mean RV of $\sim 180 \text{ km s}^{-1}$ which is on average larger than the RV derived for stellar populations within the bar, but for young main-sequence stars in the NE.

5 CONCLUSIONS

In El Youssoufi et al. (2019), we provided an updated view of the morphology of the SMC through a comprehensive age tomography. In this study, we complement their work through a homogeneous and extensive kinematic study of the different resolved stellar populations. The SMC is known to have a complicated interaction history, a complex 3D structure and an eventful star formation history; all of these factors can have an impact on the kinematics of stellar populations within the galaxy. To this end we proceed as follows:

(i) We search the ESO SAF for the best available spectra of objects belonging to the SMC, making use of NIR photometry from the VMC, VHS, 2MASS, and OGLE IV projects. Parallaxes and PMs from *Gaia* EDR3 are used to reduce the influence of MW foreground stars. The selected stars form a sample of 3700 sources. The spectra used in this study are taken with the FLAMES/GIRAFFE instrument, have an $\text{SNR} \geq 10$ and a resolving power from 6500 to 38000. The spectra are sky subtracted and a full spectrum fitting method is used to obtain RVs; the stellar spectra and their associated uncertainties were resampled onto the arbitrary wavelength grid of the templates which were taken from the X-shooter spectral library. Systematic uncertainties among the FLAMES gratings were found to be $\sim 2 \text{ km s}^{-1}$, but were not applied to correct the spectra due to not having enough combinations of gratings to homogenise the sample.

(ii) We obtain an RV distribution which shows two distinct peaks: a small peak around $18 \pm 2 \text{ km s}^{-1}$ representing the MW foreground stars in the direction of the SMC and a large peak around $159 \pm 2 \text{ km s}^{-1}$ representing stars belonging to the SMC and corresponding to a velocity dispersion (σ_v) of $33 \pm 2 \text{ km s}^{-1}$. Furthermore, we compare these values to those obtained from a homogenized RV sample of several spectroscopic studies that have previously observed SMC stars and that we anchor to the APOGEE DR17 spectra.

(iii) We find that stars occupying regions of the CMD, as defined by El Youssoufi et al. (2019), that have been poorly sampled by spectroscopic studies in the literature such as regions B (main-sequence stars 50–410 Myr old), E (faint RGB stars 2.5–8 Gyr old) and J (RC stars 2–9 Gyr old) have RVs resembling those of stellar populations of similar median ages: regions G (supergiant stars 50–230 Myr old) and K (bright RGB stars 2–8 Gyr old). On average, the RV of stellar populations younger than 500 Myr is $\sim 20 \text{ km s}^{-1}$ larger than that of stellar populations older than 2 Gyr. A similar RV dichotomy has recently been found by Mucciarelli et al. (2023) from an independent analysis of 206 RGB stars, which are also included in our sample, located on the eastern side of the galaxy around the globular cluster NGC 419. The authors characterized a metal-rich component with a large RV ($[\text{Fe}/\text{H}] \sim -0.9$ dex and $\text{RV} \sim 172 \text{ km s}^{-1}$) and a metal-poor component with a low RV ($[\text{Fe}/\text{H}] \sim -1.1$ dex and $\text{RV} \sim 154 \text{ km s}^{-1}$), suggesting that they could result from separate bursts of star formation (Massana et al. 2020).

(iv) We measure an RV difference between the Wing and bar, dominating the morphology of the SMC as traced by our sample, confirming that these two substructures are kinematically distinct. This RV difference was already noticed by Evans & Howarth (2008)

from their analysis of the kinematics of OBA type stars. PM studies corroborate this result, with the Wing kinematics following the transverse motion along the Magellanic Bridge towards the LMC (e.g. Zivick et al. 2019; Schmidt et al. 2020; Niederhofer et al. 2021). Consequently, the increased star formation rate in the Wing region following the interaction between the LMC and the SMC about 200 Myr ago (Harris & Zaritsky 2004; Rubele et al. 2015) imprinted a large RV on the newly formed stars compared to those in the bar. The Wing substructure is found to lie at a distance closer to us than the main body of the SMC, further contributing to these discrepancies (Tatton et al. 2021). The differences in kinematics between the bar and Wing are more pronounced in supergiants (150–360 Myr old; $\sim 30 \text{ km s}^{-1}$) than in young main-sequence stars (10–50 Myr old; $\sim 10 \text{ km s}^{-1}$) where the RV of stars in the bar is smaller in the former than in the latter population. Moreover, the RVs of stars in the bar are found to be larger in young main-sequence stars than in red supergiants; we attribute this to the peak of star formation in the SMC bar at ~ 40 Myr (Rubele et al. 2015) from gas already influenced by tidal stripping. This is consistent with a cold gas outflow, which is stronger in the Northern bar, that originated 33–56 Myr ago (McClure-Griffiths et al. 2018). SMC debris with large RVs has been found by Cullinane et al. (2023) at the extreme southern disc of the galaxy (6–9 deg from the centre beyond the Wing) using data from the Magellanic Edges Survey.

(v) We measure different RVs between the NE and SW portions of the bar. These differences are $\sim 10 \text{ km s}^{-1}$ and are found to be present in young populations such as main-sequence stars (10–50 Myr old) and yellow supergiants (150–360 Myr old) as well as in old populations like bright RGB stars (2–8 Gyr old). This also shows consistency between our (main-sequence and supergiant stars) and literature (bright RGB stars) studies. The NE bar region has a larger RV in young main-sequence stars than the SW region; the reverse is true for the supergiants and RGB populations. These gradients are not influenced by the projected bulk proper motion. However, we confirm a previously found rotation pattern (Dobbie et al. 2014; Di Teodoro et al. 2019; De Leo et al. 2020; Abdurro'uf et al. 2022). A prominent episode of star formation ~ 25 Myr ago is evident at the NE extremity of the bar according to Rubele et al. (2015, 2018) which coincides with the NE bar structure. In this region, there is also a predominance of young (< 140 Myr old) Cepheids in front of the main body of the SMC (Ripepi et al. 2017). The larger RV of stars in this region corroborates their formation subsequent to the gas stripping resulting from the dynamical interaction with the LMC. The largest outflow gas velocities are also found in this region (McClure-Griffiths et al. 2018). Furthermore, numerical simulations including interstellar gas dynamics and star formation processes showed that the observed structural, kinematic and stellar properties of the SMC are predominantly of tidal origin (Yoshizawa & Noguchi 2003).

(vi) Soszyński et al. (2010) and Haschke et al. (2012) noticed that RR Lyrae stars, which are distributed fairly homogeneously over the whole body of the SMC, trace two overdensities at the centre similar to those we detect from bright and faint RGB stars. Jacyszyn-Dobrzniecka et al. (2017) found similar features in the on-sky projection of the OGLE-IV data. However, the two overdensities are not present in the 3D Cartesian density maps, deducing that they might be due to a projection effect. The RR Lyrae distribution does not show any substructure or asymmetry along the line-of-sight. Furthermore, no discrepancies in the line-of-sight depth are found between the locations of the two overdensities from the analysis of RC stars (Tatton et al. 2021). In the plane of the sky, several studies based on PMs (Niederhofer et al. 2018; Zivick et al. 2019; De Leo et al. 2020) found that stars follow a non-uniform velocity structure

at the location of the SW-bar overdensity which might indicate a stretching or tidal stripping of the SMC.

In our future work, we plan to carry out a similar investigation of the stellar populations of the LMC. The upcoming large-scale spectroscopic facilities and their planned survey projects: the One Thousand and One Magellanic Fields survey (1001MC; Cioni et al. 2019) using the 4-metre Multi-Object Spectroscopic Telescope (4MOST; de Jong et al. 2019) facility at VISTA and the Survey of the Milky Way and its Satellites (Gonzalez et al. 2020) using the Multi-Object Optical and Near-infrared spectrograph (MOONS; Cirasuolo et al. 2020) facility at the VLT will significantly enlarge spectroscopic stellar sample sizes, cover large areas encompassing also the halo of the Magellanic Clouds, and increase the sensitivity to enable us to investigate substructures with kinematics, metallicity and chemistry in great detail.

ACKNOWLEDGEMENTS

This project received funding from the European Research Council (ERC), under the European Union's Horizon 2020 research and innovation programme (grant agreement no. 682115), and was supported in part by the Australian Research Council Centre of Excellence for All Sky Astrophysics in 3 Dimensions (ASTRO 3D), through project number CE170100013. We thank the Cambridge Astronomy Survey Unit (CASU) and the Wide Field Astronomy Unit (WFAU) in Edinburgh for providing the necessary data products under the support of the Science and Technology Facility Council (STFC) in the UK. This study is based on observations obtained with VISTA at the Paranal Observatory under programmes 179.B-2003 and 179.A-2010. This work has made use of data products from the Two Micron All Sky Survey, which is a joint project of the University of Massachusetts and the Infrared Processing and Analysis Center/California Institute of Technology, funded by the National Aeronautics and Space Administration and the National Science Foundation. This work has made use of data from the European Space Agency (ESA) mission *Gaia* (<http://www.cosmos.esa.int/gaia>), processed by the *Gaia* Data Processing and Analysis Consortium (DPAC; <http://www.cosmos.esa.int/web/gaia/dpac/consortium>). Funding for the DPAC has been provided by national institutions, in particular the institutions participating in the *Gaia* Multilateral Agreement. This project has made extensive use of the Tool for OPERations on Catalogues And Tables (TOPCAT) software package (Taylor 2005) as well as the following open-source Python packages: MATPLOTLIB (Hunter 2007), NUMPY (Oliphant 2015), PANDAS (McKinney 2010), SCIPY (Jones et al. 2001). We thank Marica Valentini and Salvatore Taibi for the fruitful discussions concerning the sky subtraction.

DATA AVAILABILITY

The data underlying this study are available in the ESO Archive (<http://archive.eso.org>). This concerns both catalogues to select the stellar sample and spectra to obtain the radial velocities. The *Gaia* data to establish the memberships to the SMC are also publicly available. All other data resulting from our study are made available with the publication.

REFERENCES

- Abdurro'uf et al., 2022, *ApJS*, 259, 35
 Ahumada R. et al., 2020, *ApJS*, 249, 3
 Ardeberg A., Maurice E., 1977, *A&AS*, 30, 261
 Ardeberg A., Maurice E., 1979, *A&A*, 77, 277
 Arentsen A. et al., 2019, *A&A*, 627, A138
 Bekki K., Chiba M., 2009, *PASA*, 26, 37
 Belokurov V., Erkal D., Deason A. J., Koposov S. E., De Angeli F., Evans D. W., Fraternali F., Mackey D., 2017, *MNRAS*, 466, 4711
 Boardman N. F. et al., 2017, *MNRAS*, 471, 4005
 Cappellari M., 2017, *MNRAS*, 466, 798
 Cappellari M., Emsellem E., 2004, *PASP*, 116, 138
 Carrera R., Gallart C., Aparicio A., Costa E., Méndez R. A., Noël N. E. D., 2008, *AJ*, 136, 1039
 Cioni M. R. L., Habing H. J., Israel F. P., 2000, *A&A*, 358, L9
 Cioni M.-R. L. et al., 2011, *A&A*, 527, A116
 Cioni M. R. L. et al., 2019, *The Messenger*, 175, 54
 Cirasuolo M. et al., 2020, *The Messenger*, 180, 10
 Cross N. J. G. et al., 2012, *A&A*, 548, A119
 Cullinane L. R. et al., 2020, *MNRAS*, 497, 3055
 Cullinane L. R., Mackey A. D., Da Costa G. S., Koposov S. E., Erkal D., 2023, *MNRAS*, 518, L25
 D'Onghia E., Fox A. J., 2016, *ARA&A*, 54, 363
 Dalton G. B. et al., 2006, in McLean I. S., Iye M. eds, 6269, Proc. SPIE Conf. Ser. Vol.6269, Ground-based and Airborne Instrumentation for Astronomy. SPIE, Bellingham, p. 62690X
 De Leo M., Carrera R., Noël N. E. D., Read J. I., Erkal D., Gallart C., 2020, *MNRAS*, 495, 98
 de Grijs R., Bono G., 2015, *AJ*, 149, 179
 de Jong R. S. et al., 2019, *The Messenger*, 175, 3
 de Vaucouleurs G., Freeman K. C., 1972, *Vistas Astron.*, 14, 163
 Di Teodoro E. M. et al., 2019, *MNRAS*, 483, 392
 Diaz J. D., Bekki K., 2012, *ApJ*, 750, 36
 Dobbie P. D., Cole A. A., Subramaniam A., Keller S., 2014, *MNRAS*, 442, 1663
 El Youssoufi D. et al., 2019, *MNRAS*, 490, 1076
 El Youssoufi D. et al., 2021, *MNRAS*, 505, 2020
 Emerson J., McPherson A., Sutherland W., 2006, *The Messenger*, 126, 41
 Evans C. J., Howarth I. D., 2008, *MNRAS*, 386, 826
 Gaia Collaboration et al., 2016, *A&A*, 595, A2
 Gaia Collaboration et al., 2021a, *A&A*, 649, A1
 Gaia Collaboration et al., 2021b, *A&A*, 649, A7
 Gaia Collaboration et al., 2022, preprint ([arXiv:2208.00211](https://arxiv.org/abs/2208.00211))
 Gardiner L. T., Noguchi M., 1996, *MNRAS*, 278, 191
 Gonneau A. et al., 2020, *A&A*, 634, A133
 González-Fernández C. et al., 2018, *MNRAS*, 474, 5459
 Gonzalez O. A. et al., 2020, *The Messenger*, 180, 18
 Grady J., Belokurov V., Evans N. W., 2021, *ApJ*, 909, 150
 Hardy E., Suntzeff N. B., Azzopardi M., 1989, *ApJ*, 344, 210
 Harris J., Zaritsky D., 2004, *AJ*, 127, 1531
 Harris J., Zaritsky D., 2006, *AJ*, 131, 2514
 Haschke R., Grebel E. K., Duffau S., 2012, *AJ*, 144, 107
 Hatzidimitriou D., Cannon R. D., Hawkins M. R. S., 1993, *MNRAS*, 261, 873
 Hatzidimitriou D., Croke B. F., Morgan D. H., Cannon R. D., 1997, *A&AS*, 122, 507
 Hunter J. D., 2007, *Comput. Sci. Eng.*, 9, 90
 Jacyszyn-Dobrzyniecka A. M. et al., 2016, *AcA*, 66, 149
 Jacyszyn-Dobrzyniecka A. M. et al., 2017, *AcA*, 67, 1
 Jones E., Oliphant T. E., Peterson P., et al., 2001, SciPy: Open source scientific tools for Python, <http://www.scipy.org/>
 Kallivayalil N., van der Marel R. P., Alcock C., Axelrod T., Cook K. H., Drake A. J., Geha M., 2006, *ApJ*, 638, 772
 Kallivayalil N., van der Marel R. P., Besla G., Anderson J., Alcock C., 2013, *ApJ*, 764, 161
 Katz D. et al., 2022, preprint ([arXiv:2206.05902](https://arxiv.org/abs/2206.05902))
 Koch A., Kleyna J. T., Wilkinson M. I., Grebel E. K., Gilmore G. F., Evans N. W., Wyse R. F. G., Harbeck D. R., 2007, *AJ*, 134, 566
 Kroupa P., Bastian U., 1997, *New Astron.*, 2, 77
 Kunkel W. E., Demers S., Irwin M. J., 2000, *AJ*, 119, 2789
 Lamb J. B., Oey M. S., Segura-Cox D. M., Graus A. S., Kiminki D. C., Golden-Marx J. B., Parker J. W., 2016, *ApJ*, 817, 113

- Mackey D., Kopusov S., Da Costa G., Belokurov V., Erkal D., Kuzma P., 2018, *ApJ*, 858, L21
- Majewski S. R. et al., 2017, *AJ*, 154, 94
- Martínez-Delgado D. et al., 2019, *A&A*, 631, A98
- Massana P. et al., 2020, *MNRAS*, 498, 1034
- Mathewson D. S., Cleary M. N., Murray J. D., 1974, *ApJ*, 190, 291
- Mathewson D. S., Ford V. L., Visvanathan N., 1988, *ApJ*, 333, 617
- McClure-Griffiths N. M. et al., 2018, *Nature Astron.*, 2, 901
- McKinney W., 2010, in van der Walt S., Millman J. eds, Proceedings of the 9th Python in Science Conference, p. 56
- McMahon R. G., Banerji M., Gonzalez E., Koposov S. E., Bejar V. J., Lodieu N., Rebolo R., VHS Collaboration, 2013, *The Messenger*, 154, 35
- Mucciarelli A., Minelli A., Bellazzini M., Lardo C., Romano D., Origlia L., Ferraro F. R., 2023, *A&A*, 671, 15
- Muraveva T. et al., 2018, *MNRAS*, 473, 3131
- Murray C. E., Peek J. E. G., Di Teodoro E. M., McClure-Griffiths N. M., Dickey J. M., Dénes H., 2019, *ApJ*, 887, 267
- Nidever D. L., Majewski S. R., Butler Burton W., 2008, *ApJ*, 679, 432
- Nidever D. L., Majewski S. R., Butler Burton W., Nigra L., 2010, *ApJ*, 723, 1618
- Nidever D. L., Monachesi A., Bell E. F., Majewski S. R., Muñoz R. R., Beaton R. L., 2013, *ApJ*, 779, 145
- Nidever D. L. et al., 2020, *ApJ*, 895, 88
- Niederhofer F. et al., 2018, *A&A*, 613, L8
- Niederhofer F. et al., 2021, *MNRAS*, 502, 2859
- Oey M. S. et al., 2018, *ApJ*, 867, L8
- Oliphant T. E., 2015, *Guide to NumPy*. 2nd ed., CreateSpace Independent Publishing Platform
- Omkumar A. O. et al., 2021, *MNRAS*, 500, 2757
- Pieres A. et al., 2017, *MNRAS*, 468, 1349
- Pingel N. M. et al., 2022, *PASA*, 39, e005
- Ripepi V. et al., 2017, *MNRAS*, 472, 808
- Rubele S. et al., 2015, *MNRAS*, 449, 639
- Rubele S. et al., 2018, *MNRAS*, 478, 5017
- Schmidt T. et al., 2020, *A&A*, 641, A134
- Scowcroft V., Freedman W. L., Madore B. F., Monson A., Persson S. E., Rich J., Seibert M., Rigby J. R., 2016, *ApJ*, 816, 49
- Shapley H., 1940, *Harvard Coll. Obs. Bull.*, 914, 8
- Skrutskie M. F. et al., 2006, *AJ*, 131, 1163
- Soszyński I., Udalski A., Szymański M. K., Kubiak J., Pietrzyński G., Wyrzykowski Ł., Ulaczyk K., Poleski R., 2010, *AcA*, 60, 165
- Soszyński I. et al., 2011, *AcA*, 61, 217
- Soszyński I. et al., 2015, *AcA*, 65, 297
- Soszyński I. et al., 2016, *AcA*, 66, 131
- Stanimirović S., Staveley-Smith L., Jones P. A., 2004, *ApJ*, 604, 176
- Subramanian S., Subramanian A., 2012, *ApJ*, 744, 128
- Subramanian S. et al., 2017, *MNRAS*, 467, 2980
- Suntzeff N. B., Friel E., Klemola A., Kraft R. P., Graham J. A., 1986, *AJ*, 91, 275
- Sutherland W. et al., 2015, *A&A*, 575, A25
- Tatton B. L. et al., 2021, *MNRAS*, 504, 2983
- Taylor M. B., 2005, in Shopbell P., Britton M., Ebert R., eds, ASP Conf. Ser. Vol.347, *Astronomical Data Analysis Software and Systems XIV*. Astron. Soc. Pac., San Francisco, p. 29
- van der Marel R. P., Sahlmann J., 2016, *ApJ*, 832, L23
- Vasiliev E., 2018, *MNRAS*, 481, L100
- Wilson J. C. et al., 2019, *PASP*, 131, 055001
- Yoshizawa A. M., Noguchi M., 2003, *MNRAS*, 339, 1135
- Zaritsky D., Harris J., Grebel E. K., Thompson I. B., 2000, *ApJ*, 534, L53
- Zivick P. et al., 2019, *ApJ*, 874, 78
- Zivick P., Kallivayalil N., van der Marel R. P., 2021, *ApJ*, 910, 36

SUPPORTING INFORMATION

Supplementary data are available at [MNRAS](https://www.mnras.org/) online.

[Table_1_submission.csv](#)
[table_2_submission.csv](#)

Table_4_submission_new.csv

Please note: Oxford University Press is not responsible for the content or functionality of any supporting materials supplied by the authors. Any queries (other than missing material) should be directed to the corresponding author for the article.

APPENDIX A: EXAMPLES OF SPECTRAL FITS

Fig. A1 shows the spectra of two randomly selected sources, their spectral fit obtained using pPXF, and the residuals. Each fit is the combination of a number of templates at the same RV of which the first five, with their associated parameters, are listed in Table A1 in order of weight. The sum of the weights of the templates participating to a fit is about 1.0, which means that the individual weights can be interpreted as percentage contributions to the spectrum. However, the range of stellar parameters should not be overinterpreted because first, they are not set on a regular grid and second because we have not applied regularization of the template weights, which is necessary to attach a physical interpretation to the results. Nevertheless, the 1.2 arcsec aperture of the MEDUSA fibres would, in dense stellar regions like the Magellanic Clouds, collect the flux from more than just one source. This might be captured by the pPXF method similarly to what happens in the observation of nearby galaxies with integral field spectrographs for which the pPXF method was originally designed.

Source ADP.2019-02-01T01_00_32.982 is represented by a hot stellar spectrum. It is located in CMD region B and it is most likely a main-sequence star. The resulting RV is of 112.9 km s^{-1} . Source ADP.2019-10-23T14_43_58.789 is represented by a rather

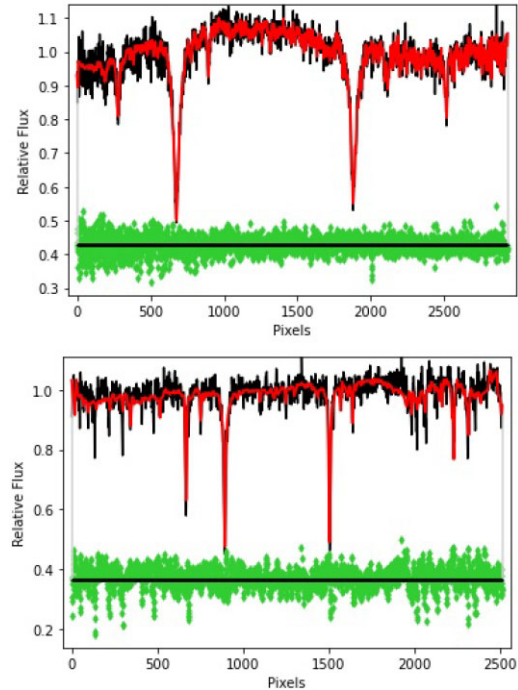
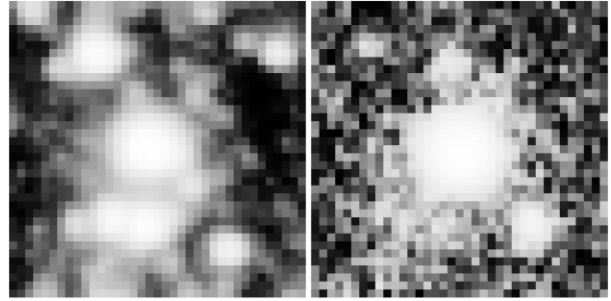


Figure A1. Spectra, spectral fits and residuals for sources ADP.2019-02-01T01_00_32.982 (top) and ADP.2019-10-23T14_43_58.789 (bottom).

Table A1. Spectral templates and their parameters contributing to the pPXF-based fits of two sources.

Template	T_{eff} K	$\log(g)$ cm s^{-2}	[Fe/H] dex	weight
Source ADP.2019-02-01T01_00_32.982:				
HD 38856 (X0817)	15 659	4.18	−0.04	0.23
HD 149382 (X0692)	34 165	5.54	−1.16	0.20
HD 176301 (X0676)	14 552	3.77	0.26	0.11
HD 170783 (X0470)	15 500	3.63	0.29	0.10
HD 43286 (X0539)	16 006	4.16	−0.11	0.06
Source ADP.2019-10-23T14_43_58.789:				
HE 1201–1512 (X0622)	5729	3.59	−2.61	0.40
HD 4359 (X0448)	17 340	4.86	−0.04	0.39
NGC 1904 223 (X0523)	4226	0.69	−1.42	0.25
HE 1207–3108 (X0630)	5435	3.24	−2.65	0.23
HD 4539 (X0463)	17 303	4.84	−0.04	0.18

**Figure A2.** Post-stamp $0.2 \times 0.2 \text{ arcmin}^2$ K_s -band images of sources ADP.2019-02-01T01_00_32.982 (left) and ADP.2019-10-23T14_43_58.789 (right).

heterogeneous set of template spectra. It is located in CMD region E and it is most likely a RGB star. The resulting RV is of 146.6 km s^{-1} . Fig. A2 shows that both sources have neighbouring sources and/or nebulous emission suggesting a possible contamination of their spectra.

This paper has been typeset from a $\text{\TeX}/\text{\LaTeX}$ file prepared by the author.